Atomization and Sprays 20(4), 311–336 (2010)

DETAILED NUMERICAL INVESTIGATION OF TURBULENT ATOMIZATION OF LIQUID JETS

O. Desjardins[1,*] & H. Pitsch[2]

[1]*Department of Mechanical Engineering, University of Colorado at Boulder, Boulder, Colorado 80309*

[2]*Department of Mechanical Engineering, Stanford University, Stanford, California 94305*

[*]Address all correspondence to O. Desjardins E-mail: desjardi@colorado.edu

Original Manuscript Submitted: 02/11/2009; Final Draft Received: 08/3/2010

A detailed numerical investigation of turbulent liquid jets in quiescent air is conducted, with the focus on the processes leading to liquid atomization. Spectral refinement of the interface is employed to provide an accurate description of the phase interface, even at the subcell level. The ghost fluid method is used to handle the different material properties of the phases and the surface tension force in a sharp manner. A temporally evolving turbulent planar jet is simulated for several values of the Reynolds and Weber numbers, and statistics are extracted. Direct visualization of the flow structures allows one to lay out a clear picture of the atomization process. Early interface deformation is caused by turbulent eddies that carry enough kinetic energy to overcome surface tension forces. Then, liquid protrusions are stretched out into ligaments that rupture following Rayleigh's theory or due to aerodynamic forces. This numerical study provides a wealth of much-needed detailed information on the turbulent atomization process, which is invaluable to large eddy simulation modeling.

KEY WORDS: *primary atomization, turbulence, DNS, incompressible flow, level set, ghost fluid, planar jet*

1. INTRODUCTION

1.1 Background and Motivation

Atomization, or the process by which a coherent liquid disintegrates into droplets, is a fundamental topic of fluid mechanics and has numerous engineering, environmental, as well as pharmaceutical applications. Among the many engineering applications, the atomization of liquid fuels that occurs in energy conversion devices is of great importance because it governs the size of fuel droplets, their subsequent evaporation rate, and therefore will affect the homogeneity of the mixture. As a consequence, fuel atomization will have far-reaching repercussions on many different aspects of the combustion process, such as pollutant formation. To improve the design of energy conversion devices through computational methods, predictive models for atomization have to be provided. Figure 1 shows a sketch of the liquid atomization process. Although models are available for the so-called secondary atomization, (i.e., the breakup of small liquid drops or structures into smaller droplets), the description of primary atomization (i.e., the disintegration of a coherent liquid core into drops) is not as mature, and few models are available to describe this phenomenon. This represents one of the main bottlenecks in numerical modeling of combustion devices today.

Many reasons explain why primary atomization remains such a challenging topic. First, the complex flows associated with liquid breakup involve turbulence, surface

1044–5110/10/$35.00

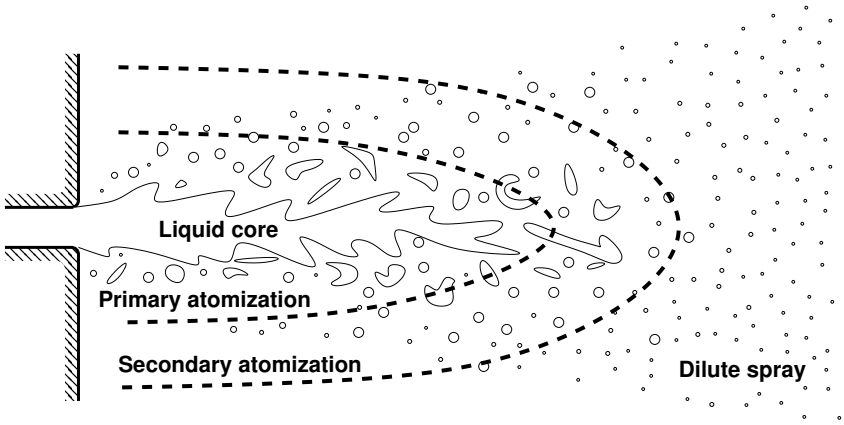

FIG. 1: Schematics of the atomization process of a liquid jet.

tension effects, and potentially large density ratios. Then, the difficulty associated with modeling is due to the importance of small liquid scales in combustion systems: modeling primary atomization means modeling a process by which mass and energy are transferred from the large liquid scales to small liquid structures. In this process, the interest is mostly in the size distribution of small liquid scales, which determines the evaporation rate. Primary atomization and the subsequent secondary breakup might not follow a cascade process, where new structures are produced only on the largest scales. Furthermore, the production of large-scale structures might not be in equilibrium with small droplet evaporation, because of the long time scales involved. These observations differ greatly from standard Kolmogorov theory-based turbulence modeling.

Although a consensus has been reached in identifying the mechanisms behind certain atomization problems, many fundamental aspects of primary atomization remain poorly understood to this day. Hence, numerous questions remain, such as what mechanisms govern the turbulent atomization of liquid jets in quiescent air, or whether a coherent liquid core can be found in realistic liquid injection applications. Also, it is unclear whether the classical understanding of a primary liquid breakup followed by a secondary breakup is appropriate. To all these questions, numerical simulations can provide much needed answers, provided the numerical algorithms are made sufficiently reliable.

1.2 Previous Work

1.2.1 Experimental Work

A large body of experimental work exists on the topic of atomization. Because numerical modeling is so limited and because the theory behind atomization is complex, experiments have been the main means of study in this field. However, many challenges are also limiting the progress in experimental understanding of the physics of atomization. Indeed, the dispersed liquid phase limits optical access to the liquid core, and the scales involved in these flows are typically very small. As a result, experiments often aim at gathering statistical data on the droplets that result from the atomization process, instead of looking at the initial phase of the liquid breakup (Smallwood and Gülder, 2000).

However, for numerous simpler two-phase flow problems, such as droplet splashing, binary drop collision, or single-droplet breakup, abundant detailed experimental work has been published. For example, the issue of how a single droplet undergoes secondary breakup has been carefully analyzed by Chou and Faeth (1998). Droplet splashing and the well-known milk crown phenomenon have been studied extensively as well [see, e.g., Yarin (2006) for a review on the topic]. Binary drop collisions have been visualized and classified, for example, by Ashgriz and Poo (1990). Such problems are of great interest for they are likely to play a role in the complex process of liquid atomization. However, they can be seen as secondary because they rely on the assumption that droplets are already present in the system.

On the topic of how these droplets are initially generated (i.e., primary atomization itself), much less experimental studies are available. A specific topic on which a precise theory is available is the case of air-blast atomization (i.e., atomization caused by a fast coflowing gas stream). In this configuration, the mechanisms leading to drop formation have been clearly identified by Hopfinger, Villermaux, and coworkers [see, e.g., Lasheras and Hopfinger (2000), Marmottant and Villermaux (2004),

Villermaux (2007)]. They suggested that the interface is first subject to a Kelvin-Helmholtz instability, leading to a longitudinal wave being formed on the surface of the jet. Then, as this wave grows, it undergoes a secondary instability of Rayleigh-Taylor type. This leads to the generation of bulges at the top of the wave crest. These liquid bulges are then picked up by the fast coflowing gas and stretched into thin ligaments that ultimately undergo Rayleigh breakup and droplet formation. However, these investigations were limited to laminar flows, as well as high-density ratios.

Concerning the issue of high-speed liquid injection in a quiescent environment, experiments have yet to provide a complete picture of the atomization mechanisms. A series of studies by Faeth et al. (1995) and Sallam et al. (2002) have shed some light on the complex phenomena that take place at the surface of the liquid jet by using pulsed shadowgraphs. Their results suggest that the turbulence of the liquid field is of crucial importance in the development of the interfacial structures. Moreover, they were able to provide models for the breakup length, the onset of turbulent breakup, and the resulting droplet velocity. However, most of these correlations where obtained for high-density ratios (on the order of 1000), in which case they observed that aerodynamics forces had little impact on the liquid structures. On the contrary, Wu and Faeth (1993) suggested that, for a density ratio of <500, aerodynamic effects start to influence the breakup. Because most engineering applications involve significantly smaller density ratios (on the order of 40 for diesel injection, 100 for aircraft engines), it is expected that aerodynamic forces should be essential in the atomization process in many practical combustion devices. In this case, breakup was found to be enhanced, leading to smaller droplets, and secondary breakup was found to merge with primary atomization. Note that the idea that aerodynamic forces can contribute to the breakup of liquid jets originates from classical work on non-turbulent atomization by Levich (1992) and Taylor (1963).

Recently, novel techniques based on x-ray visualization have emerged, suggesting that significant progress will be made in experimental visualization of turbulent atomization. Such x-ray visualization has been employed by Wang et al. (2008) to investigate the near-field gasoline direct injection (GDI) process under realistic conditions. The assessment of the breakup mechanisms was beyond the scope of their work; however they reported observing the formation of membranes and related this fact to mechanisms of air-blast atomization presented by Lasheras and Hopfinger (2000). In the near future, these new techniques should allow one to characterize more precisely the coherent liquid core under engine conditions.

1.2.2 Numerical Work

Because primary atomization represents a challenge for experimentalists, numerical modeling should provide a much needed alternative. However, numerical studies of primary atomization have also been very sparse. To simulate two-phase flows, various techniques have been developed, which all enjoy some benefit and suffer from limitations. Because no clear gold standard has emerged on how to conduct a numerical simulation of complex two-phase flows, the number of direct numerical studies of primary atomization remains limited. Several key issues remain, such as the discontinuous nature of the flow properties across the phase interface, the singularity of the surface tension forces, and the very large range of scales involves in atomization. Thus far, all the simulations of turbulent primary atomization published have in common their severe underresolution. De Villiers and Gosman (2004) and Bianchi et al. (2007; 2005) conducted large-eddy simulation (LES) of the diesel injection, but no subgrid scale (SGS) model for the interfacial physics was employed. It is unlikely that such an approach could provide much information on the atomization process. Ménard et al. (2007) simulated a similar problem without SGS models, but with significantly lower Reynolds and Weber numbers. However, it is still unclear whether their simulation was properly resolved. Also, they relied on upwinded schemes and numerical dissipation to ensure the robustness of their simulations. Finally, Pan and Suga (2006) simulated laminar breakup in the Rayleigh regime, but their simulations did not involve turbulent atomization.

In parallel to these efforts, several numerical studies aimed at understanding the linear stability of liquid jets through the solution of the Orr-Sommerfeld equation. Yecko et al. (2002) and Boeck and Zaleski (2005) provided some detailed analysis of the numerous instability modes, and their relative importance. Such studies are fundamental in the detailed understanding of the theory of breakup; however, they are limited to the early destabilization of the liquid interface under the assumption of a parallel flow and therefore cannot fully characterize the mechanisms of turbulent atomization.

In summary, the fully turbulent breakup of a liquid jet has been considered only rarely, and never has it been simulated using numerical methods designed for turbulence. To successfully tackle this problem, one must care-

fully combine each of several key ingredients, including numerical methods capable of simulating turbulence properly, an accurate description of the gas-liquid interface, and a robust approach to handle the discontinuous material properties between the two phases.

1.2.3 Modeling Work

An overview of past research on the topic of primary atomization would be incomplete without an account of conventional phenomenological models. The objective of such models is to reproduce statistically the main features of the atomization process with modest computational requirements. Many different modeling strategies have been proposed, based for example, on surface instabilities (Patterson and Reitz, 1998), drop shedding (Yi and Reitz, 2004), or cavitation (Kong et al., 1999). However, these models replace the atomization process by the injection of round liquid blobs directly at the nozzle exit, and therefore, they cannot be expected to provide accurate results close to the nozzle. In addition, such models typically assume a main atomization mechanism that might not be adequate in all situations, suggesting that fine-tuning the models against experiments might be necessary. Two novel strategies in phenomenological modeling are also of interest and should be reported here. They attempt to bridge the existing gap between overly expensive detailed simulations and oversimplified particle-based phenomenological models, while remaining practically applicable. First, Gorokhovski (2001) proposed to perform stochastic modeling of primary atomization considering the liquid jet depletion as a fragmentation cascade with scaling symmetry. Second, Vallet et al. (2001) proposed to solve a transport equation for the mean interface density in the context of Reynolds-averaged Navier-Stokes (RANS). These two approaches, along with some selected results, are reviewed in Gorokhovski and Herrmann (2008) and seem promising.

1.3 Objectives

This work attempts to improve the understanding of primary atomization through detailed numerical simulations. Numerical techniques have matured rapidly in the past few years, and the associated increase in computational power allow to perform fine simulations of complex turbulent problems. By carefully choosing the simulation parameters, turbulent atomization can be simulated, with reasonable confidence in the numerics. The choices made here are detailed in Section 2. This work has several objectives as follows:

- Establish numerical simulations has a realistic means of study of turbulent atomization
- Visualize primary atomization, and compare the computed results to available experimental observations
- Identify key atomization mechanisms
- Analyze the effect of the jet Reynolds number
- Analyze the effect of the Weber number
- Investigate the statistics of a turbulent liquid jet

This work is considered a first step toward realistic applications. The density ratio employed is similar to that of Diesel injection. The Reynolds number is slightly reduced compared to realistic injectors, however still of the right order of magnitude. The Weber number is reduced manyfold in order to make the liquid structures tractable on a fixed mesh.

Naturally, all conclusions drawn in this paper are only valid for the limited range of parameters explored here. Simulations at higher Reynolds and Weber numbers will need to be conducted in order to generalize these findings. Needless to say, conducting direct numerical simulation of primary atomization with realistic parameters will remain out of computational reach for many years, but the information extracted from lower Reynolds and Weber number simulations should provide useful information to guide model development.

2. MATHEMATICAL FORMULATION

To simulate turbulent two-phase flows, the incompressible Navier-Stokes equations are introduced

$$\frac{\partial \boldsymbol{u}}{\partial t} + \boldsymbol{u}\cdot\nabla\boldsymbol{u} = -\frac{1}{\rho}\nabla p + \frac{1}{\rho}\nabla\cdot\left(\mu\left[\nabla\boldsymbol{u} + \nabla\boldsymbol{u}^{\mathrm{T}}\right]\right) + \boldsymbol{g} \quad (1)$$

where $\boldsymbol{u}$ is the velocity field, ρ is the density, p is the pressure, $\boldsymbol{g}$ is the gravitational acceleration, and μ is the dynamic viscosity. The continuity equation can be rewritten in terms of the incompressibility constraint

$$\frac{\partial \rho}{\partial t} + \nabla\cdot(\rho\boldsymbol{u}) = \frac{\partial \rho}{\partial t} + \boldsymbol{u}\cdot\nabla\rho = 0 \quad (2)$$

The interface Γ separates the liquid from the gaseous phase. The material properties in each phase are constant,

but differ between the phases. Thus, we write $\rho = \rho_l$ in the liquid phase and $\rho = \rho_g$ in the gas phase. Similarly, $\mu = \mu_l$ in the liquid and $\mu = \mu_g$ in the gas. At the interface Γ, the jumps in material properties are written $[\rho]_\Gamma = \rho_l - \rho_g$ and $[\mu]_\Gamma = \mu_l - \mu_g$ for the density and the viscosity, respectively. Because the velocity field is continuous, $[\boldsymbol{u}]_\Gamma = 0$. However, the pressure displays a jump between the two phases that can be written

$$[p]_\Gamma = \sigma\kappa + 2\,[\mu]_\Gamma\, \boldsymbol{n}^{\mathrm{T}} \cdot \nabla \boldsymbol{u} \cdot \boldsymbol{n} \tag{3}$$

where σ is the surface tension coefficient, κ is the interface curvature, and $\boldsymbol{n}$ is the interface normal.

3. NUMERICAL METHODOLOGY

3.1 Navier-Stokes Solver

The flow solver used in this work is NGA. This solver and the numerical methods it uses was extensively described in Desjardins et al. (2008a). This solver was originally designed for direct numerical simulations (DNS) and large eddy simulations (LES) of complex, turbulent, reactive flows. Consequently, it is based on numerical methods that are discretely mass, momentum, and energy conserving, in order to avoid all numerical dissipation that is known to be detrimental to the simulation of turbulence (Desjardins et al., 2008a; Park et al., 2004). Although NGA allows for arbitrarily high spatial accuracy, the current simulations are performed using second-order spatial discretization. The temporal integration is based on the second-order accurate, semi-implicit iterative Crank-Nicolson scheme of Pierce and Moin (2001). These techniques have often been used with great success to conduct detailed numerical studies of various turbulent flows (Desjardins and Pitsch, 2006; Knudsen and Pitsch, 2008, 2009; Wang, 2007).

3.2 Spectrally Refined Interface Approach

In order to avoid having to transport the discontinuous density field, Eq. (2) is replaced by a more convenient equation (i.e., the so-called level set equation), which allows one to track the interface location as an iso-contour G_0 of a smooth function G. By solving

$$\frac{\partial G}{\partial t} + \boldsymbol{u} \cdot \nabla G = 0 \tag{4}$$

Various numerical techniques have been devised to solve Eq. (4). Most importantly, a level set methodology requires an accurate transport of the interface location, even at the smallest resolved scales. Also of great importance is the capability of a level-set scheme to provide an accurate interfacial curvature. Recently, a spectrally refined interface (SRI) approach was developed (Desjardins et al., 2008b) that satisfies these two constraints by enabling a subcell resolution of the interface. By introducing a number of collocation points in each grid cell, SRI provides a polynomial reconstruction of the level-set function G. The resulting approach essentially removes mass conservation issues that are known to plague level-set methods and provide excellent accuracy of the interface transport even at the smallest resolved scales.

3.3 Ghost Fluid Method

The discontinuous material properties of the flow as well as the singular surface tension force are treated using the ghost fluid method (GFM) of Fedkiw et al. (1999). GFM enables an accurate description of the flow at the interface, by treating all discontinuities in a sharp manner. The idea behind this method is to use standard differentiation operators across discontinuous variables by extending them using Taylor series expansions, and then to add the jumps explicitly. This results in an efficient and robust method that treats all the difficulties associated with two-phase flows with good accuracy. The results of several test cases in previous publications (Desjardins et al., 2008b; Desjardins and Pitsch, 2009) suggest that GFM provides good accuracy even on very few ($<$10) grid points, for canonical problems such as Rayleigh breakup, Rayleigh-Taylor, or the decay of a standing wave. Therefore, this approach seems appropriate to handle the small structures that are expected in primary atomization.

4. TURBULENT PLANAR JET

4.1 Flow Configuration

The flow considered in this section consists of a temporally evolving planar liquid jet in quiescent air. Although most realistic injection devices rely on round nozzles, the computational requirement of a planar jet simulation is typically lower because of the additional homogeneous periodic direction. Naturally, some features of round liquid jets, such as Rayleigh instabilities, will be missing from the planar jet simulations; however, it is expected that most aspects of the flow will be identical. Figure 2 shows a sketch of the flow configuration. The liquid jet is initially of height H, and its bulk velocity is U_0. The computational domain is periodic in the streamwise and spanwise directions, x and z, respectively, while in

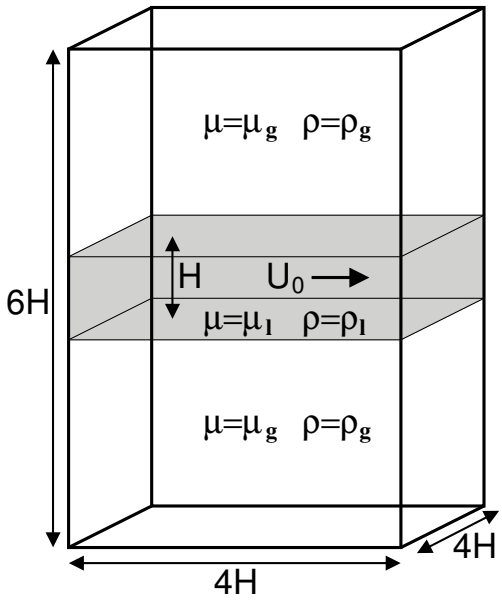

FIG. 2: Schematics of the temporally evolving planar jet.

the y direction, a symmetry condition is employed. The $4H \times 6H \times 4H$ domain is discretized on a $256 \times 384 \times 256$ uniform mesh, leading to $\Delta x = \Delta y = \Delta z = H/64$. The initial velocity is obtained from a precursor simulation of a periodic channel flow. This precursor simulation is conducted in a $4H \times H \times 4H$ domain, discretized on a $256 \times 192 \times 256$ mesh, using the liquid material properties. Once the flow is established (i.e., once the friction coefficient reaches a constant value), the simulation is stopped and the velocity field is recorded. This field is then interpolated on the jet mesh to initialize the velocity in the region $-H/2 < y < H/2$, while the velocity outside of this region is set to zero. Even though the initial coexistence between a turbulent liquid and a still gas is a greatly simplified representation of turbulent liquid injection, the presence of realistic turbulence ensures that the planar jet destabilizes and develops rapidly. Throughout this work, time $t^\star$ will be nondimensionalized using $t = t^\star U_0/H$.

The parameters used for the simulations are summarized in Table 1. The density ratio is set to $\rho_l/\rho_g = 40$, which corresponds to what is typically observed in diesel engines, and which is sufficiently low to avoid any numerical difficulties. The choice is made to take $\mu_l/\mu_g = 40$, leading to $\nu_l = \nu_g$. Both the Reynolds number, $\mathrm{Re} = \rho_l U_0 H/\mu_l$, and the Weber number, $\mathrm{We} = \rho_l U_0^2 H/\sigma$, are varied such that both the effect of turbulence and the effect of surface tension forces can be studied. The Ohnesorge number, $\mathrm{Oh} = \mu_l/\left(\rho_l H \sigma\right)^{1/2}$, is also reported in Table 1 for the various cases. Clearly, the Ohnesorge number remains small for all cases, meaning that the liquid viscosity should not play any significant role throughout the atomization process, which is expected to be the case for diesel injection. Figure 3 places the different cases studied on the Ohnesorge chart, first introduced by Ohnesorge (1936), then improved by Reitz (1978), Lefebvre (1989), and Miesse (1955). Note that all the cases considered here lie within the so-called second wind-induced breakup regime. However, as noted by (1989), a fully turbulent liquid jet will be immediately disrupted because of the nonzero vertical velocity component, leading to a global turbulent disintegration of the liquid. As a result, it is expected that the cases studied here will all undergo turbulent atomization.

TABLE 1: Flow parameters for the various planar jet simulations.

Case	ρ_l/ρ_g	μ_l/μ_g	Re	We	Oh
$TPa1$	40	40	3000	500	0.007454
$TPa2$	40	40	2000	500	0.011180
$TPb1$	40	40	3000	1000	0.010541
$TPb2$	40	40	2000	1000	0.015811
$TPc1$	40	40	3000	2000	0.014907
$TPc2$	40	40	2000	2000	0.022361

4.2 Resolution Considerations

In order to ensure the adequate resolution of the flow for the various simulation parameters, several issues have to be considered. Obviously, the smallest turbulent scales need to be properly resolved by the flow solver mesh. In addition, the liquid structures have to be resolved as well, which might lead to an even more restricting constraint on the mesh size. Indeed, small ligaments and droplets are expected to form, as well as potentially extremely thin sheets. Strictly speaking, the only true cutoff scale for the liquid structures is the actual phase-interface thickness, which is clearly too small to be resolvable by the approach followed here. This specific aspect of multiphase flows represents a difficult challenge, and current state-of-the-art methods in two-phase flow modeling remain far from being able to tackle problems such as the formation of small satellite droplets, bag breakup of liquid sheets, or drainage of gas layers between two liquid

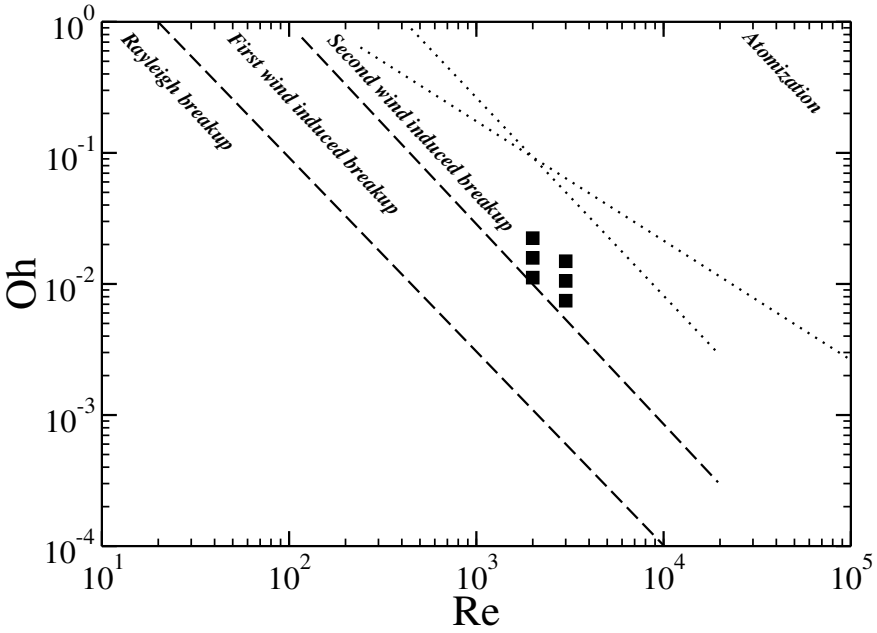

FIG. 3: Cases considered in this work (symbols, see Table 1 for details) placed on the Ohnesorge chart for liquid jet breakup.

structures before collision. However, all these phenomena are expected to occur regularly during the turbulent atomization of a liquid jet. As a consequence, the notion of DNS of multiphase flows remains controversial. The assumption behind the work presented here is that the main features of turbulent atomization can be simulated with reasonable accuracy, without accounting for the extremely small scales associated with two-phase flows, provided that most scales are properly resolved. Although this assumption is typically valid for turbulence simulations, where the fluctuating energy decreases as smaller scales are considered, it might not be adequate for two-phase flows, where small liquid structures can carry a lot of momentum, and small-scale phenomena can govern the outcome of large-scale events, as in the case of binary drop collision. Even with these limitations in mind, the present work can provide valuable insights on the physics of primary atomization, as well as on the capability of sharp level-set-based methods to predict turbulent breakup.

The resolution of the turbulence is related to the number of grid points per jet height H, 64 in the present work, as well as the Reynold number Re, 2000 or 3000 here. This is comparable to numerous previous studies of temporal and spatial jets. Stanley et al. (2002) performed a DNS of a spatial jet at $\mathrm{Re} = 3000$ using 30 mesh points within the jet height and found the smallest value for the Kolmogorov scale, defined by $\eta = \left(\nu^3/\epsilon\right)^{1/4}$ where ϵ is the dissipation, to be $\eta \approx \Delta x/3$. Da Silva and Pereira (1998) computed a temporally evolving planar jet at $\mathrm{Re} = 3000$, using 48 mesh points inside the jet height, and reported finding $\Delta x/\eta \approx 3$. Assuming a classical scaling for the number of points across the jet height proportional to $\mathrm{Re}^{3/4}$, these previous studies suggest that even the cases at $\mathrm{Re} = 5000$ should be properly resolved with 64 points per H. Although this analysis is valid for single-phase jets, it is yet unclear whether similar scalings apply in the presence of two phases. As a consequence, we limit ourselves to a Reynolds number of 3000 to ensure proper resolution of the turbulence.

The resolution of the liquid scales will be assessed following the consideration of Ménard et al. (2007), who proposed to introduce a grid-based Weber number defined by $\mathrm{We}_{\Delta x} = \rho_l U_0^2 \Delta x/\sigma$. This corresponds to the Weber number of the smallest resolvable liquid structure, assuming that such a structure is of the order of the mesh size Δx. Ménard et al. (2007) suggested that if $\mathrm{We}_{\Delta x}$ is smaller than about 10, then no further breakup is expected from a liquid structure of the size of the mesh. This limit of 10 for the Weber number matches the experimental observations of Hsiang and Faeth (1992). Although this is a convincing argument for a droplet or a ligament, it

does not apply easily to a liquid sheet, for which breakup could still obviously occur. This brings us back to the previous part of the discussion on what can realistically be resolved in complex two-phase flow simulations. In our case, because the SRI approach provides subcell interfacial resolution, structures as small as $\Delta x/p$, where p is the order of the polynomials used in the level-set function reconstruction, should become tractable, at least in the sense that they should be maintained and transported, even though the flow around them might not be properly captured. This suggests that another Weber number, $\mathrm{We}_{\Delta x/p} = \rho_l U_0^2 \Delta x/(p\sigma)$, should be defined as well. For the different Weber numbers We considered in this study, Table 2 presents these two mesh-based Weber numbers, considering that p is set to 5. For all cases, the subcell Weber number is well below 10, suggesting that most liquid scales should remain tractable throughout the simulations. In addition, the grid-based Weber number remains low, which should be sufficient to ensure the accuracy of the flow around most liquid structures. This can be further assessed by directly evaluating the liquid mass conservation errors as a function of time, as shown in Fig. 4. Small mass loss should suggest that indeed most liquid structures are properly resolved at all times. For all three $\mathrm{Re} = 3000$ cases, which are expected to be the most challenging simulations in terms of resolution, the mass conservation errors are found to remain below 2% for $t < 30$. This value is considered here to be sufficiently small to confirm that the chosen numerical parameters lead to a properly resolved flow.

5. STATISTICAL RESULTS

First, statistical results will be analyzed. Although we are interested in the detailed mechanisms of breakup, which should be easier to analyze and understand from instantaneous results, averaged data on a multiphase jet have almost never been reported and therefore are of great interest.

TABLE 2: Grid-based Weber numbers for the different cases simulated.

We	$\mathrm{We}_{\Delta x}$	$\mathrm{We}_{\Delta x/p}$
500	7.8125	1.5625
1000	15.625	3.1250
2000	31.250	6.2500

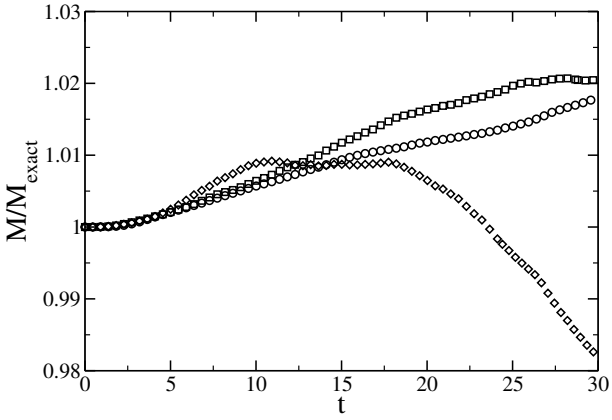

FIG. 4: Temporal evolution of the liquid mass normalized by the exact liquid mass in the domain for $\mathrm{Re} = 3000$: $\mathrm{We} = 500$ (circles), $\mathrm{We} = 1000$ (squares), and $\mathrm{We} = 2000$ (diamonds).

5.1 Jet Growth

First, the jet half-width based on the longitudinal velocity is plotted in Fig. 5. The width of the jets is expressed as the half-width δ_U, defined as the distance from the jet centerline to the point at which the mean streamwise velocity excess is half of the centerline velocity. It can be seen that after $t \approx 5$, the growth rate of all jets is close to linear, although some deviation is clearly visible. These fluctuations in the jet half-width can be attributed to several aspects of the present simulations, such as the lateral confinement leading to a small statistical sample size, and to the low Reynolds numbers. Also, note that surface tension effects are expected to affect the development of the jets. This can be seen by comparing the growth rate of the jets for different Weber numbers. High Weber number jets grow faster, whereas low Weber number jets tend to have a slower growth, which suggests that surface tension forces tend to stabilize the jets. It can be observed that the growth rates of the jets decrease when the half-widths reach $2H$, which suggests that confinement in the y direction prevents further development of the fluid structures. As a result, further analysis will be limited to $t < 30$, for which we can expect the y boundaries to remain sufficiently far from the jets.

5.2 Volume Fraction Statistics

Figure 6 shows the temporal evolution of the mean liquid volume fraction in the $\mathrm{Re} = 3000$ jets. Again, the stabilizing effect of surface tension forces appears clearly be-

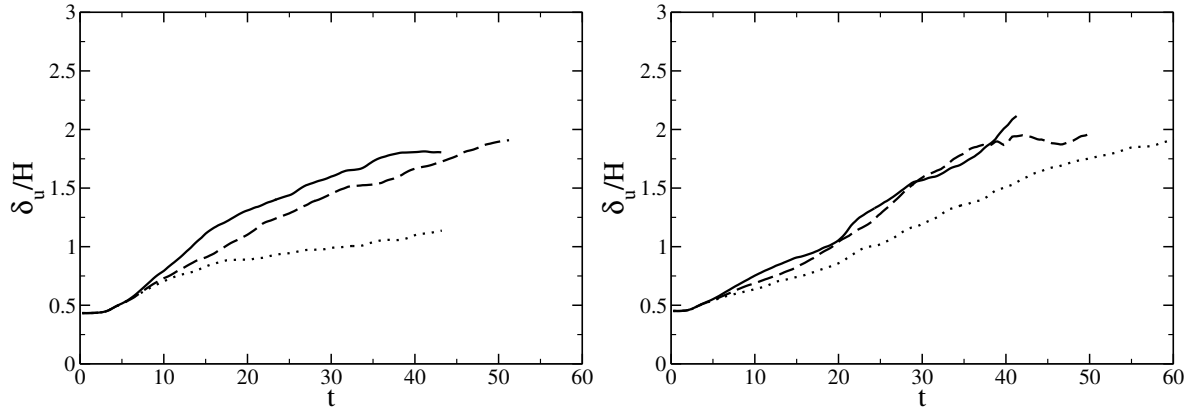

(a) Re = 2000 (b) Re = 3000

FIG. 5: Time evolution of jet half-width: We $= 500$ (dotted line), We $= 1000$ (dashed line), and We $= 2000$ (solid line).

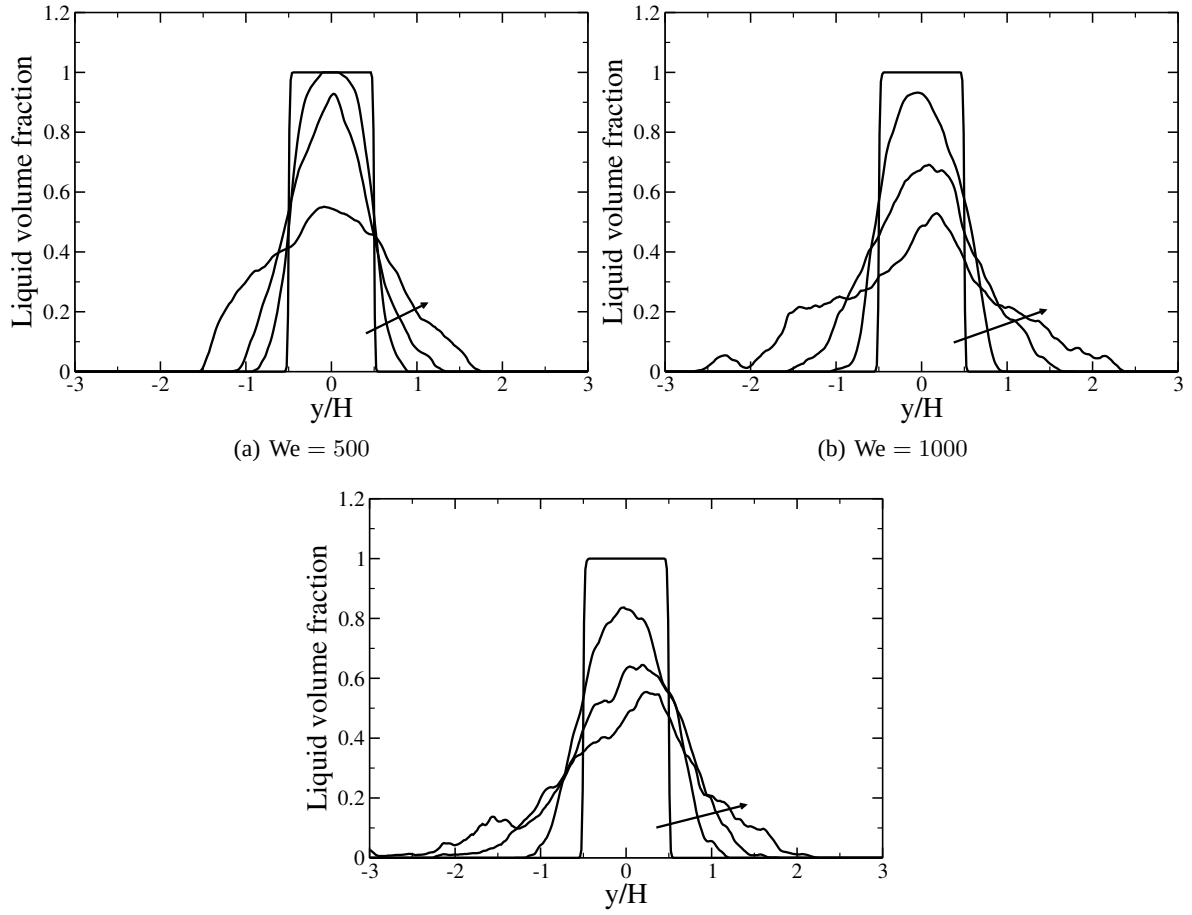

(a) We $= 500$ (b) We $= 1000$

(c) We $= 2000$

FIG. 6: Mean profiles of liquid volume fraction for the planar jets at different times for Re $= 3000$ and various Weber numbers. Arrows indicate increasing time ($t = 1, 10, 20, 30$).

cause the spreading of the volume fraction profiles is significantly reduced for lower Weber numbers. In all cases, at $t = 30$ the mean liquid volume fraction at the center of the jet is $\sim$0.5, suggesting that as much gas as liquid is present in the core of the jet at this time. Note that for larger Weber numbers, the liquid occupies almost the entire computational domain at $t = 30$, which confirms that vertical confinement effects could become important after this time. Figure 7 shows the rms profiles of the liquid volume fraction. For all cases, at later times, it can be noted that the rms becomes large within the jet core itself, which is in part due to the existence of gas bubbles that have been entrapped in the liquid. Later, in the higher Weber number simulations, the growth of liquid protrusions leads to the formation of holes in the liquid core, when the interface from both sides of the jet merges. On the gas side, the large rms values are due initially to the presence of numerous protrusions, then to the development of ligaments.

5.3 Velocity Statistics

The mean longitudinal velocity is plotted at four different times for Re $= 3000$ and for various Weber numbers in Fig. 8. The velocity is normalized by the centerline velocity, and the y coordinate is normalized by the jet half-width. With this normalization, a similar single-phase jet would show self-similar behavior in the time interval where a linear growth rate is observed. Here, it can be noted that the collapse of normalized profiles at different times is not perfect, especially for the low Weber number case, for which surface tension effects are stronger. However, for high Weber numbers, it appears that the velocity profiles collapse rather well, which suggests that

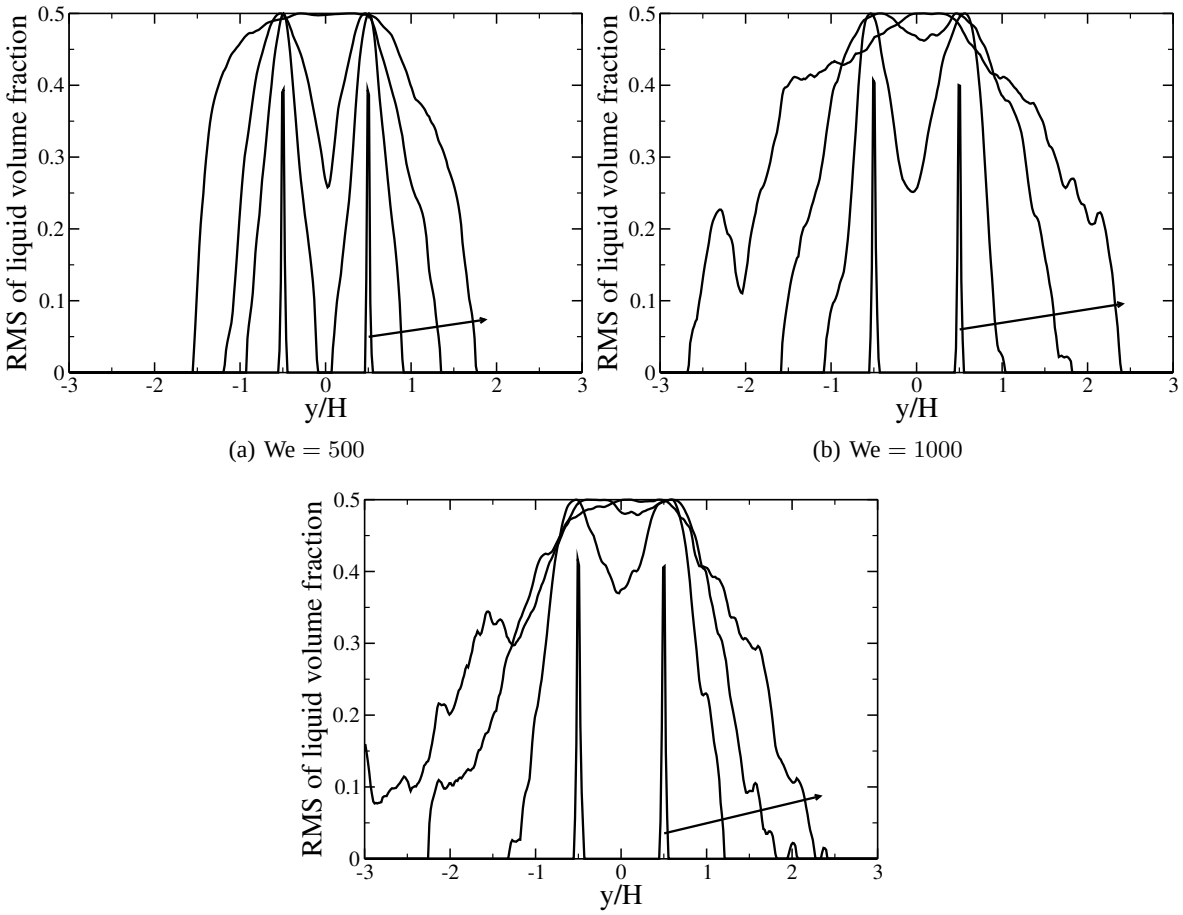

(a) We $= 500$

(b) We $= 1000$

(c) We $= 2000$

FIG. 7: Rms profiles of liquid volume fraction for the planar jets at different times for Re $= 3000$ and various Weber numbers. Arrows indicate increasing time ($t = 1, 10, 20, 30$).

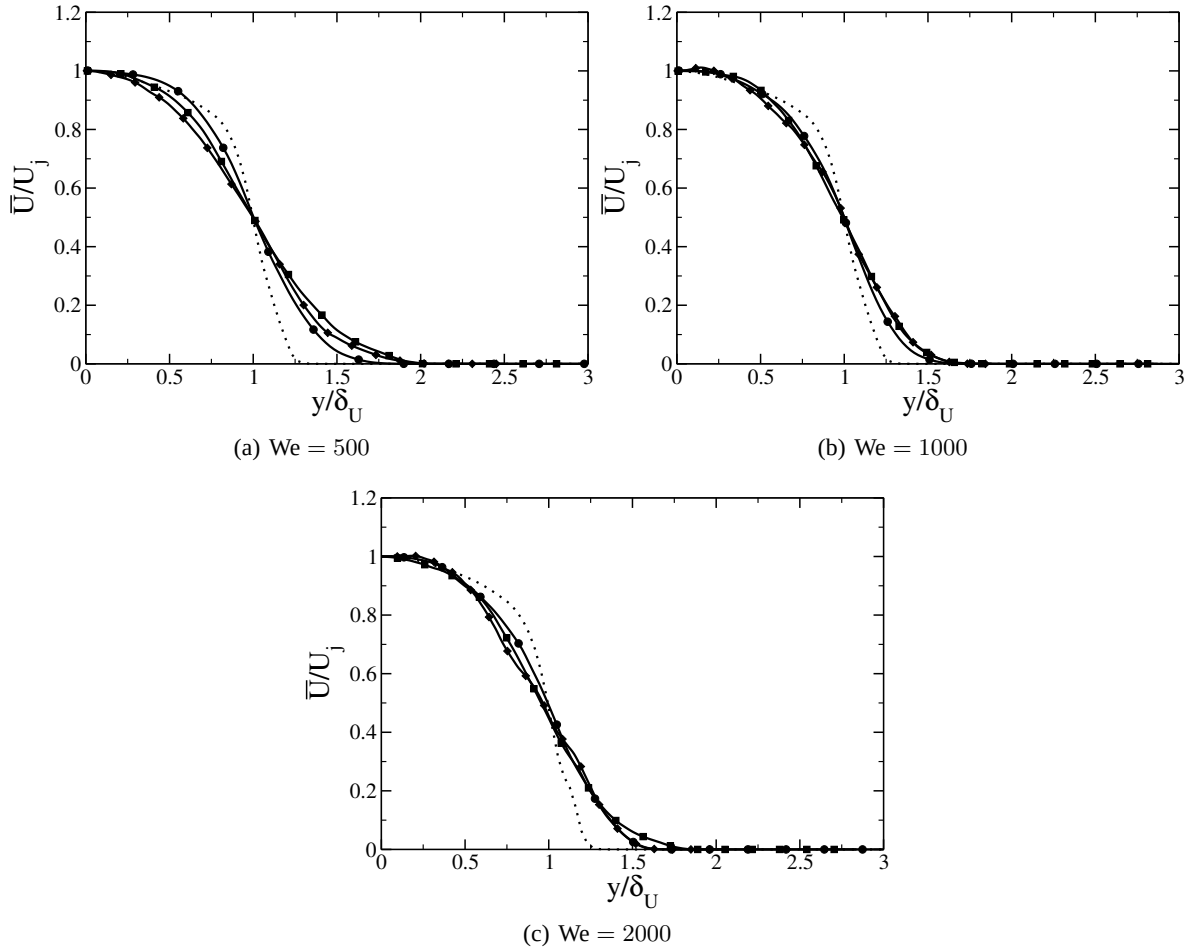

(a) We $= 500$ (b) We $= 1000$

(c) We $= 2000$

FIG. 8: Mean profiles of streamwise velocity of the planar jets at different times for Re $= 3000$ and various Weber numbers: $t = 1$ (dotted line), $t = 10$ (circles), $t = 20$ (squares), and $t = 30$ (diamonds).

two-phase jets display a self-similar nature when surface tension forces are not dominating.

In order to investigate the mean flow field in more detail, the mean streamwise velocity conditioned on the phase is shown in Fig. 9 for Re $= 3000$ and for various Weber numbers. A clear difference can be observed between the liquid velocity and the gas velocity, regardless of the Weber number. In all cases, the liquid is associated with a larger mean velocity than the gas. This is expected, since initially all the momentum is carried by the liquid. As the jets undergo breakup, the liquid ligaments and droplets tend to retain a larger velocity than the surrounding gas. It should be noted that this effect is more pronounced with the lowest Weber number jet, for which the mean axial liquid velocity is 75% larger than the mean gas velocity at the jet half-width. This can be attributed to the fact that this jet undergoes little disruption because of the larger surface tension forces. As a result, momentum exchange between phases tends to remain limited. For the largest Weber number, the mean axial liquid velocity is $<$40% larger than the mean gas velocity at the jet half-width, indicating that momentum exchange between the phases is enhanced by the intense disruption of the jet.

Figure 10 shows the Rms profiles of the axial velocity for the same cases. Regardless of the Weber number, these profiles show a large peak around the jet half-width. Such strong maxima in streamwise velocity fluctuations are not observed in single phase jets (Stanley et al., 2002), and are likely due to the interaction of the turbulent eddies with the phase-interface, as well as with the surface tension force. Indeed, the amplitude of these peaks decreases with increasing Weber number.

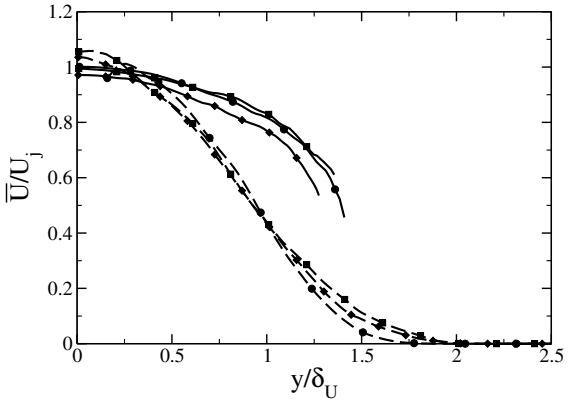

(a) We $= 500$

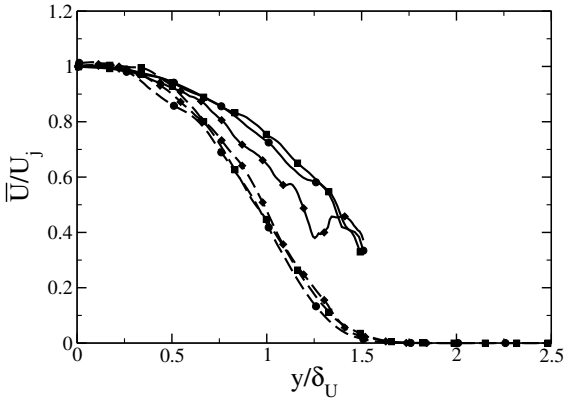

(b) We $= 1000$

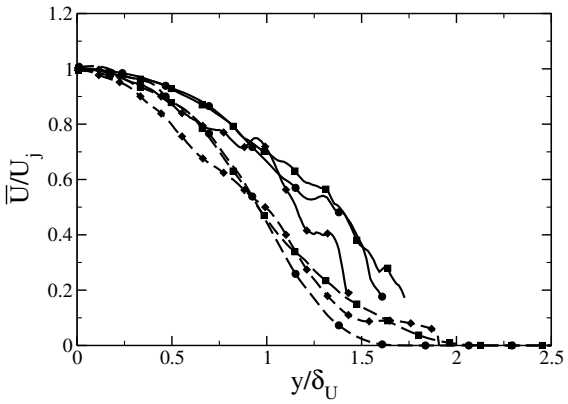

(c) We $= 2000$

FIG. 9: Phase-conditioned mean profiles of streamwise velocity of the planar jets at different times for Re $= 3000$ and various Weber numbers: liquid phase (solid lines) and gas phase (dash lines) at $t = 10$ (circles), $t = 20$ (squares), and $t = 30$ (diamonds).

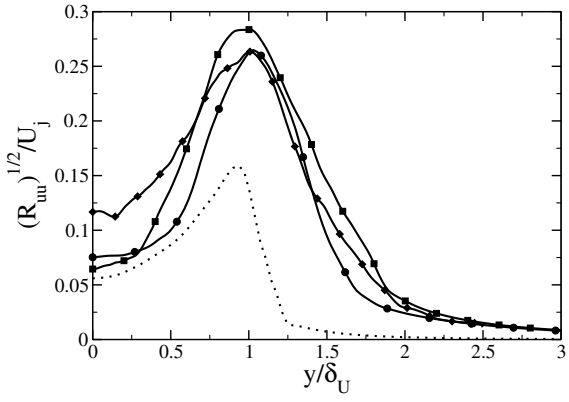

(a) We $= 500$

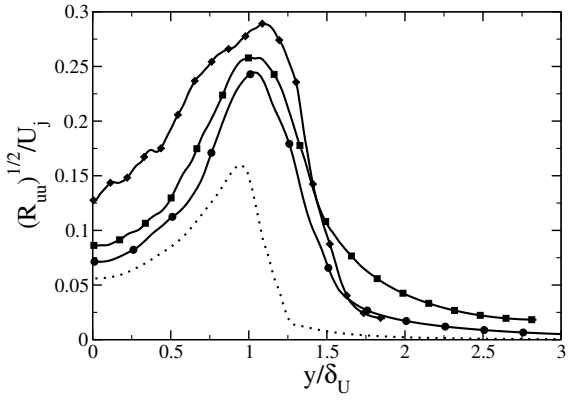

(b) We $= 1000$

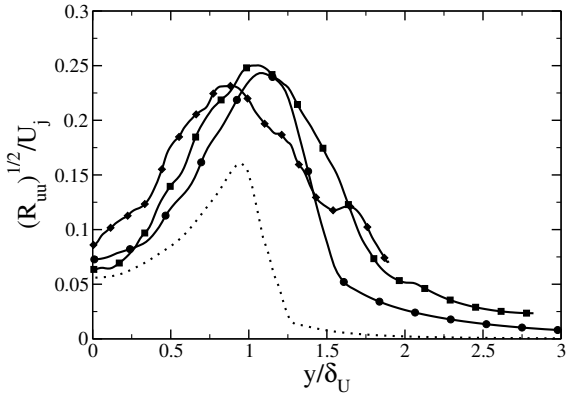

(c) We $= 2000$

FIG. 10: Rms profiles of streamwise velocity of the planar jets at different times for Re $= 3000$ and various Weber numbers: $t = 1$ (dotted line), $t = 10$ (circles), $t = 20$ (squares), and $t = 30$ (diamonds).

Finally, Fig. 11 shows the longitudinal energy spectrum E_{11} as a function of the wave number k for case $TPb1$ at three different times during the course of the simulation. These spectra are computed at $y = \delta_U$. Note

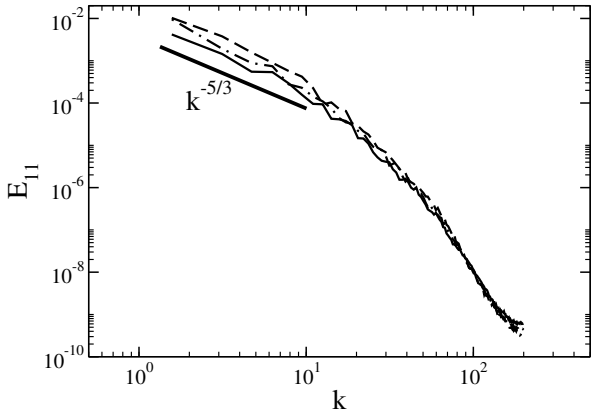

FIG. 11: Streamwise energy spectrum at $y = \delta_U$ for planar jet $TPb1$ at different times: $t = 10$ (dashed line), $t = 20$ (dashed-dotted line), and $t = 30$ (solid line).

that we recover almost a decade with a $k^{-5/3}$ slope, indicating that this jet is fully turbulent. As time increases, the turbulent kinetic energy decreases slowly because of viscous dissipation.

6. INSTANTANEOUS RESULTS

6.1 Global Description of the Flow

In this section, the global features of the flow for jet $TPb1$ are first described. Figure 12 presents a three-dimensional view of the phase interface at different times during the development of the liquid jet. As expected, because of the initially turbulent liquid, the interface starts wrinkling immediately after the beginning of the run. These corrugations then grow and complex phenomena become apparent, such as the entrapment of air bubbles within the liquid jet or the wrapping of liquid sheets around eddies. As the interfacial structures become larger, individual ligaments are being stretched. Typically, they are found to be oriented in the $(-x)$ direction. These ligaments eventually rupture and form droplets. It should be noted that the disruption of the jet as well as the formation of droplets is dominated by these ligaments. The disruption of the jet does not display a cascade nature, where the jet would first breakup into big structures, then into smaller structures. The fact that most droplets are generated through the rupture of preexisting ligaments is essential to the atomization process and has been recurrently observed and documented (Villermaux, 2007). From the results of these simulations, a clear picture of the atomization already emerges that can be summarized in three essential steps:

- Initial corrugation of the interface
- Formation and stretching of liquid ligaments
- Rupture of these ligaments, leading to droplet formation

It is interesting to note that Kelvin-Helmholtz (KH) instabilities are not visible at early times, potentially due to the predominance of turbulent fluctuations, or to the fact that they have not been sufficiently amplified. Yet, numerous droplets have already been generated. This suggests that the liquid turbulence plays an important role in the generation of the first droplets. As the jet keeps developing, a large-scale KH-type wave becomes visible and greatly enhances the generation of ligaments, sheets, and droplets. However, this wave appears late in the simulation and might be caused by the confinement of the liquid jet, both in the streamwise and lateral directions. The numerous liquid ligaments, crests, and droplets observed in the simulation results are qualitatively in good agreement with experimental observations by Faeth et al. (1995).

Figure 13 shows an iso-surface of the Q-criterion, which is the second invariant of the velocity gradient tensor. This quantity has been widely used to help visualize coherent vortical structures (Dubief and Delcayre, 2000; Hunt et al., 1988). The iso-surface at $Q = 5$ is shown because it allows one to visualize the main structures of the flow while retaining the clarity of the figure. This value will be used for all Q-criterion iso-surfaces in this section. Between the first two images, the nature of the flow structures changes strongly. At $t = 2.5$, both vortex streaks, expected from wall-bounded flows, and flat vortices that are aligned in the streamwise direction are found. The nature of these structures will be examined more closely below. At $t = 7.5$ and later on, the vortices resemble the wormlike structures expected for well-developed jet turbulence. The size of the largest structures increases with time, as turbulence develops. From the first three images, KH-type waves cannot clearly be observed, suggesting that they probably do not play a significant role. However, it becomes noticeable at later times that a KH longitudinal fluctuation is present. The full turbulent nature of this flow appears clearly, and a wide range of structure sizes interact within each shear layer at first, then between the two shear layers at later times.

Comparing the simulation results with experimental observations that have been reported in the literature, two main differences can be noted. First, Sallam et al. (1999) reported that the ligaments they observed in their jets were randomly oriented, rather than preferentially oriented in

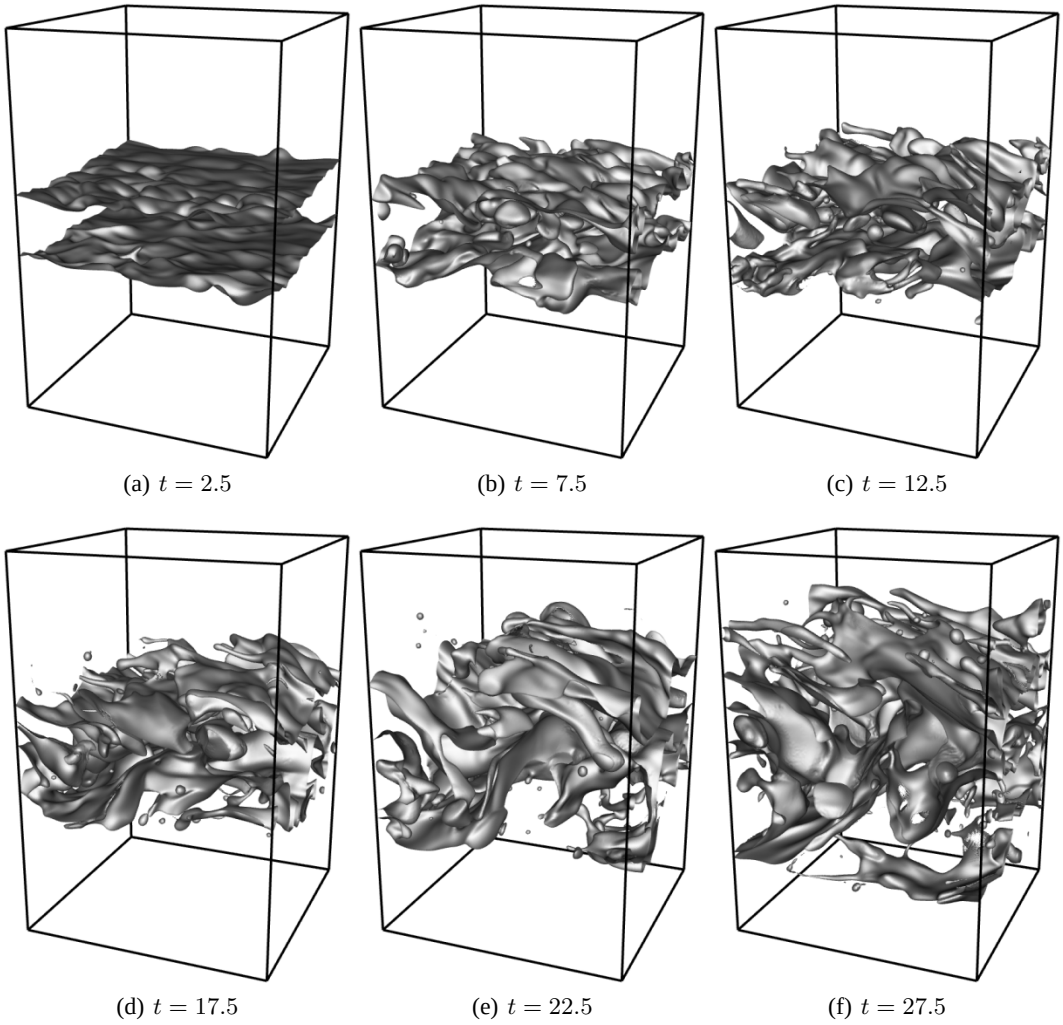

(a) $t = 2.5$ (b) $t = 7.5$ (c) $t = 12.5$

(d) $t = 17.5$ (e) $t = 22.5$ (f) $t = 27.5$

FIG. 12: Instantaneous phase-interface location at different times for case $TPb1$.

the $(-x)$ direction. They attributed this fact to the small importance of aerodynamic forces in relationship with the large density ratio they were using. Here, because the density ratio is much lower, aerodynamic forces on the liquid structures are expected to be significant. The aerodynamic forces acting on the protruding liquid ligaments cause them to be deflected toward the $(-x)$ direction, which was experimentally observed for a density ratio of the order of 100 by Wu and Faeth (1993). These differences are of great interest, because liquid atomization in many combustion devices, such as diesel engines and gas turbines, involves such small density ratios. The present results might therefore be more relevant for these applications. Second, Sallam et al. (1999) reported not observing any bubble in the region where the interface was sufficiently undisturbed to allow for direct visualization. In contrast, the present simulations show gas bubbles trapped in the liquid. Again, this difference is likely to be caused by the importance of aerodynamic effects in the simulations, which will be shown below to greatly enhance the interface deformation.

6.2 Effect of the Weber Number

The effect of the surface tension forces is discussed by comparing a top view $(+y)$ of the interface at different Weber numbers. Cases $TPa1$, $TPb1$, and $TPc1$ are considered for this purpose. Figure 14 shows this top view at the times $t = 5$, 15, and 25. For the earliest time, a significant difference between the three interfa-

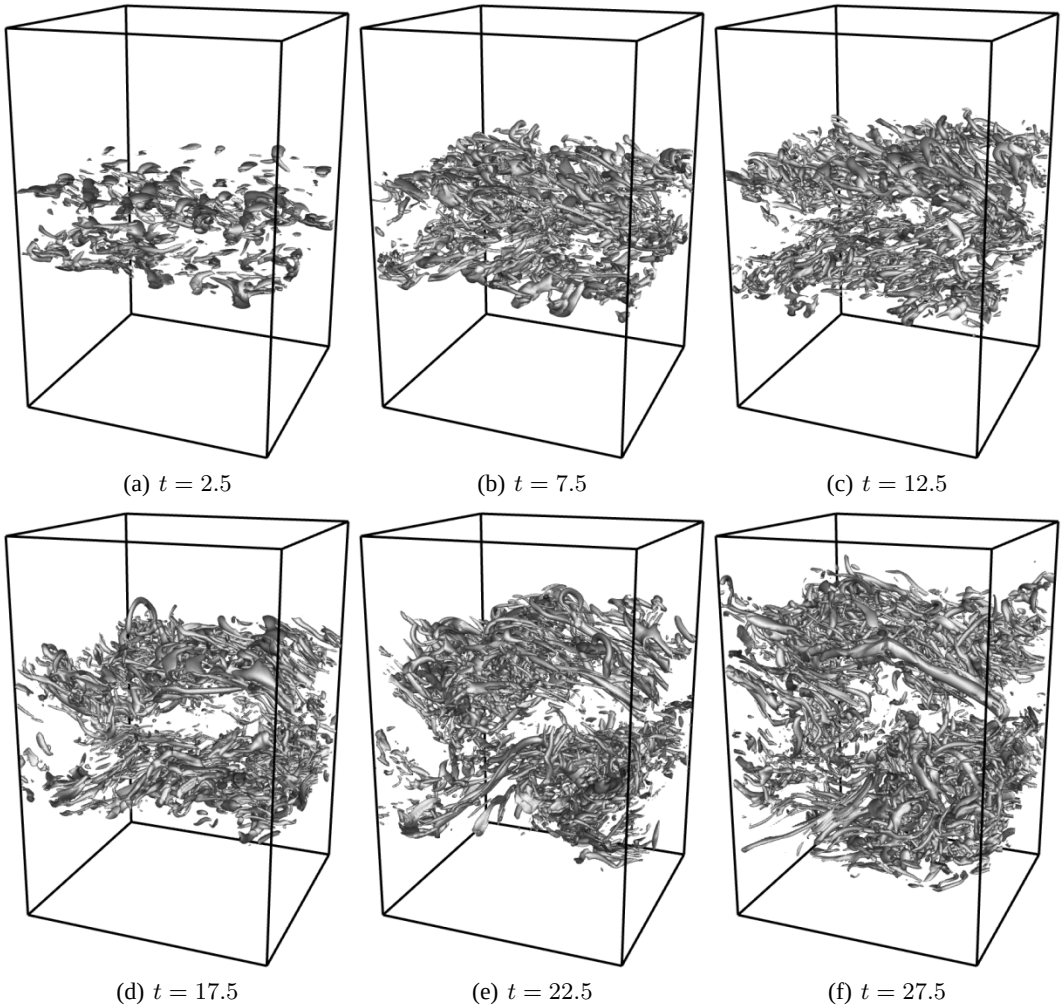

(a) $t = 2.5$ (b) $t = 7.5$ (c) $t = 12.5$

(d) $t = 17.5$ (e) $t = 22.5$ (f) $t = 27.5$

FIG. 13: Instantaneous normalized Q-criterion at different times for case $TPb2$: $Q = 5$ iso-surface is shown.

cial shapes can be noted for the different Weber numbers. The interface roughness is much lower for We $= 500$ than for We $= 2000$, which is expected because surface tension forces work against the deformation of the interface. Clearly, at this time, the large-scale structures are still very similar for the three different cases, indicating that the large-scale turbulent eddies carry enough energy to induce interfacial deformation despite surface tension forces. Smaller scales become much more apparent for high Weber numbers, which suggests that surface tension forces act as a cutoff in interfacial structure length scales. For a high Weber number, even small turbulent scales, which carry less kinetic energy, can deform the interface, while for a low Weber number, only energetic scales are able to disrupt the interface. The observation of the interfaces at later times confirms this analysis, and in general the low Weber number interface remains much less disturbed than the high Weber number interface. Note that similarities between the structures for various Weber numbers have mostly disappeared at $t = 15$. Regardless of the Weber number considered, droplets are generated through the creation and stretching of liquid ligaments. Ligaments are longer, thinner, and more numerous as the Weber number is increased. The same remark can be made concerning droplets, which tend to be smaller and more abundant for the high Weber number case than for the low Weber number case. Finally, it should be noted that the sizes of ligaments and droplets become larger at later times in all cases, which has been observed also by Sallam et al. (1999), and

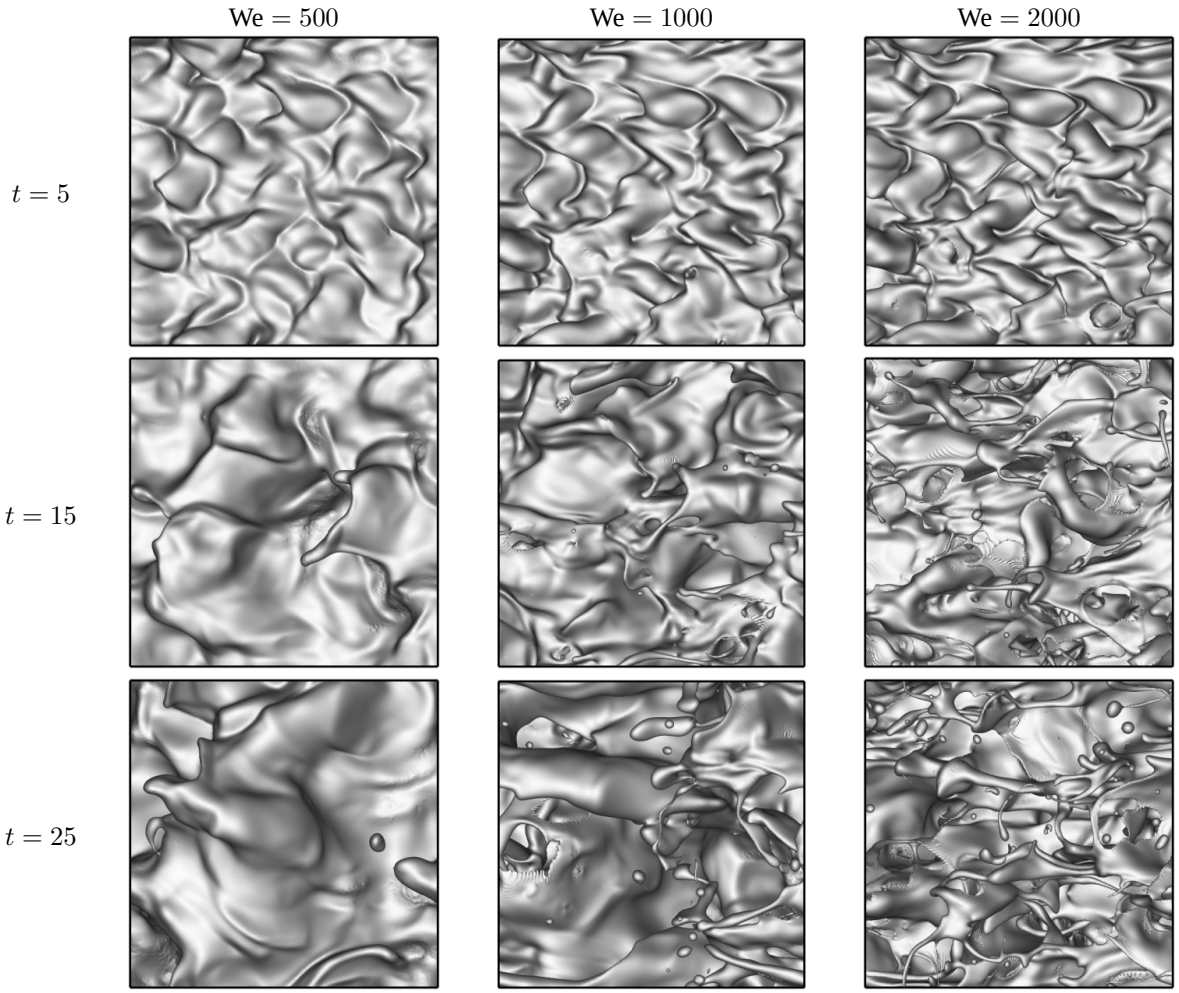

FIG. 14: Top view of the interface for Re $= 3000$ as a function of time and Weber number.

can be attributed to the dissipation of the small turbulent scales.

6.3 Effect of the Reynolds Number

In order to assess the effect of the Reynolds number on the interface disruption, two different Reynolds numbers have been considered. Although it is unclear whether many lasting differences will emerge between Re $= 2000$ and Re $= 3000$, the difference in the level of turbulence should at least impact the early deformation of the interface. Figure 15 compares the interface for cases $TPb1$ and $TPb2$ at different times throughout the simulations. Clearly, the later development of the various liquid structures is very similar between the two Reynolds numbers. The resulting ligaments appear to be of the same size, and the droplets seem similar in size and number. This observation suggests that the processes by which ligaments are stretched out and ruptured are not significantly affected by changing the Reynolds number. Of course, the range of scales found in Re $= 2000$ turbulence and Re $= 3000$ turbulence is rather limited; therefore, it is possible that changing the Reynolds number more significantly could have a stronger effect. Note that Sallam et al. (1999) reported that increasing the injection velocity (i.e., increasing both the Reynolds number and the Weber number at the same time) led to little consequences on the largest liquid structures, while smaller and more numerous small scales were obtained. The main difference between the two simulations can be found in the earliest interface visualization, where the corrugation length scales appear larger for the low Reynolds number case. This is to be ex-

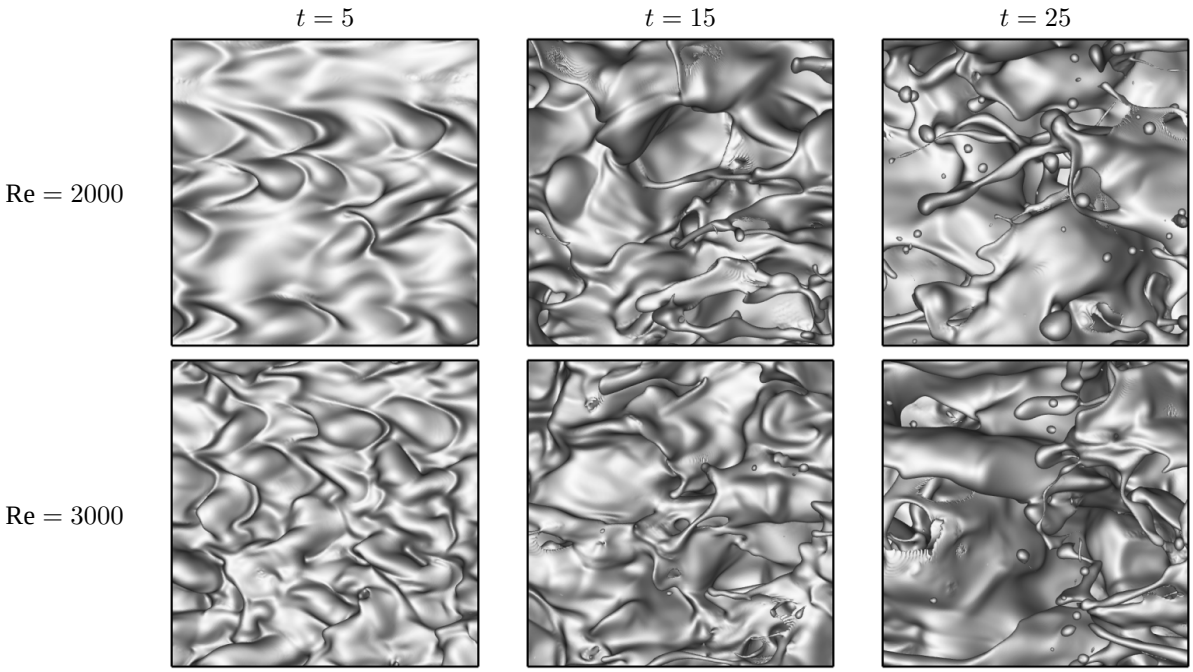

FIG. 15: Top view of the interface for We $= 1000$ as a function of time and Reynolds number.

pected, considering that less energy is contained in small eddies for the low Reynolds number case compared to the larger Reynolds number case. Consequently, the early deformation on the smaller scales of the interface is more likely to take place on relatively larger length scales as the Reynolds number is reduced.

6.4 Onset of Atomization

The early destabilization of the phase-interface is now discussed in more details. Figure 16 shows the temporal evolution of both interface location and iso-surface of Q-criterion for case $TPb1$, at early times. At $t = 0.25$,

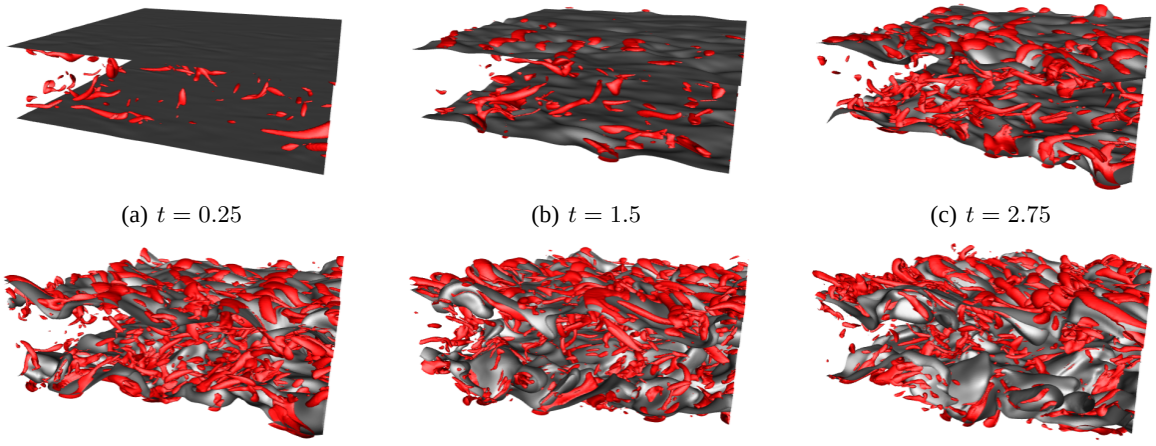

(a) $t = 0.25$ (b) $t = 1.5$ (c) $t = 2.75$

(d) $t = 4$ (e) $t = 5.25$ (f) $t = 6.5$

FIG. 16: Time evolution of phase-interface (gray) and iso-surface of Q-criterion (red) for Re $= 3000$ and We $= 1000$ for early times.

the interface has barely started to deform, and the turbulent structures clearly resemble wall-bounded turbulence, with the characteristic vortex tubes inclined ∼45 deg from the interface, where the wall used to be (Kim, 1983; Kim and Moin, 1986; Kim et al., 1987). As the simulation progresses and reaches $t = 1.5$, the interface begins to display some corrugations. While the liquid flow structures remain very similar to wall-bounded turbulence, the occurrence of flat structures in the gas should be noted. These structures appear at the phase-interface surface, mostly aligned in the spanwise direction. At $t = 2.75$, these gas structures become more pronounced. From a close examination of the interface, it can be noted that these spanwise structures are always found where the interface displays a hump toward the gas. At this time, the turbulence within the liquid layer has evolved significantly from wall-bounded turbulence, with more numerous structures, and increased complexity in their shape and alignment. This can be attributed to the interactions that start to take place with the interfacial corrugations, which have reached a significant size. In order to better understand the nature of the spanwise-aligned structures found in the gas stream, Fig. 17 shows a vertical view of the interface and of an iso-surface of Q-criterion, colored by the axial component of the vorticity, both from the liquid and gas sides. The difference between the structures on the liquid side and on the gas side appears clearly. The liquid side contains small tubular vortices that resemble wall-bounded flow structures. They are mostly aligned with the flow direction and display either a positive or a negative axial vorticity, which implies that they rotate about the x-axis, in one direction or the other. On the contrary, the gas structures are mostly flat eddies slightly stretched in the spanwise direction, and they show small levels of axial vorticity. This suggests that these structures are recirculation regions formed on top of the protruding interface, therefore containing mostly spanwise vorticity. This observation can be related to the aerodynamic effects discussed earlier. As the vertical component of the velocity field leads to interfacial corrugations, the gas phase is required to flow around the protruding liquid eddies. This process will form an area of low pressure and generate lift on the liquid eddy. As the liquid obstacle rises even higher, local recirculation regions are likely to form in the gas phase. At later times, Fig. 16 shows that as this lift effect accentuates the interfacial deformation, more complex structures are formed, both in the liquid and gas phases. The description of aerodynamic effects at the onset of turbulent atomization was first proposed through phenomenological analysis in Wu and Faeth (1993) in order to provide an explanation for the fact that smaller droplets were obtained when lower density ratios were used in atomization experiments. In the present simulations, this theory is clearly validated, and stands out as a central element of turbulent primary breakup. Figure 18 shows two sketches that illustrate the initial deformation of the interface and the mechanism through which lift enhances interfacial disruption. In Fig. 18, L is the turbulent

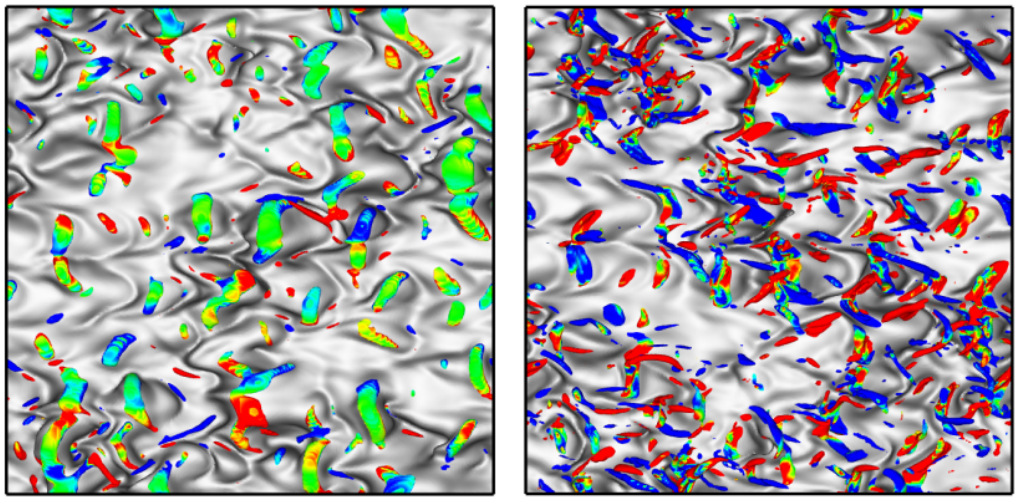

(a) From gas side. (b) From liquid size.

FIG. 17: Time evolution of phase-interface (grey) and iso-surface of Q-criterion (red) for Re $= 3000$ and We $= 1000$ for early times.

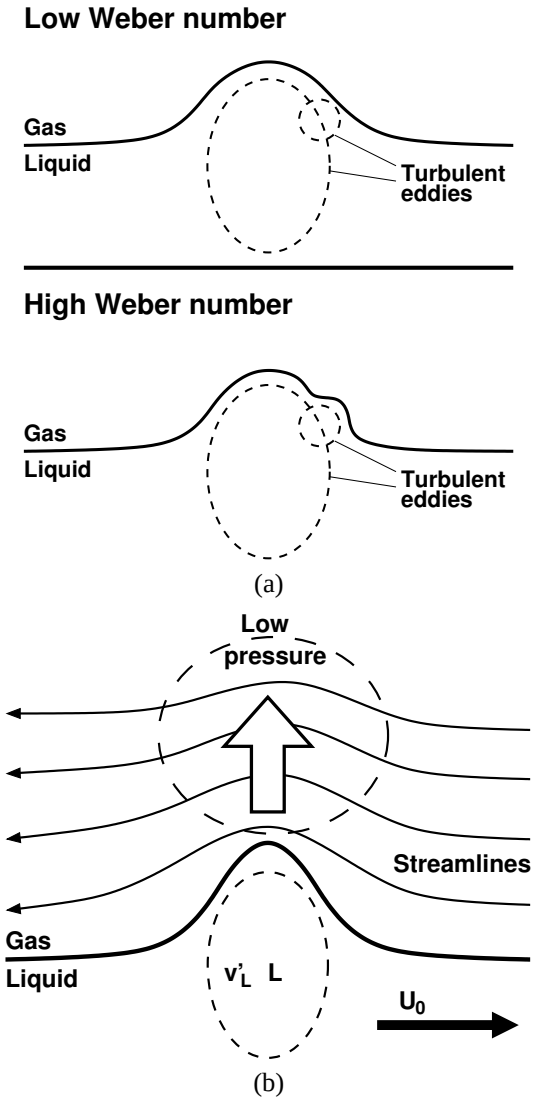

FIG. 18: Schematics of the mechanisms leading to turbulent breakup: early deformation of the interface due to vertical turbulent velocity (a), and aerodynamic enhancement of breakup through lift effect (b).

eddy size, v'_L the associated turbulent vertical velocity, and it is assumed that the liquid structure moves at the bulk jet velocity U_0. Estimates for the scaling of the different effects interacting here were first used in Wu and Faeth (1993) to relate the expected drop diameter to the Weber number, and is reiterated here for the sake of completeness. Per unit volume, the following can be written:

- Kinetic energy of the liquid structure: $E_K \sim \rho_l {v'_L}^2$
- Energy added through aerodynamic lift: $E_L \sim \rho_g {U_0}^2$
- Energy associated with surface tension: $E_{ST} \sim \sigma/L$

E_L and E_K need to overcome E_{ST} in order to lead to breakup. If the density ratio is large, then it seems safe to neglect aerodynamic lift. The important effects are then the turbulent kinetic energy in the vertical direction versus the stabilizing effect of surface tension. Clearly, if v'_L is such that $E_K > E_{ST}$, then the interface is expected to deform. In the inertial subrange, ${v'_L}^3/L \sim \epsilon$; therefore, E_K can be expressed as $E_K \sim \rho_l \epsilon^{2/3} L^{2/3}$. For smaller values of L, E_{ST} will increase while E_K will decrease, meaning that surface tension forces will act as a cutoff in the interfacial perturbation length scales by preventing small eddies that carry little energy to deform the interface. If the density ratio is smaller, then E_L will contribute to the destabilization of the interface, enabling smaller structures to deform the interface.

On the topic of early ligament formation, it should be noted that the actual shape of the liquid structures that are removed from the central liquid core depends on the form of the turbulent eddy that initiated its development. Also, this shape is affected by the surrounding turbulent structures, leading to a very complex behavior. Because of the three-dimensionality of the initial wall-bounded turbulent flow, the interface tends to initially form compact humps that protrude in the gas, leading to ligaments. However, wider liquid structures are also formed, leading to liquid crests. These crests often produce several ligaments, but occasionally generate thin sheets. These sheets have very complex dynamics that warrant further investigation. Note that they seem to be more strongly affected by aerodynamic effects and that their rupture leads to the recovery of one or several ligaments. It seems unlikely that these sheets are properly resolved in the present simulations; therefore, drawing any conclusions on their physics is difficult. However, their existence can probably be related to bag breakup events that have been observed experimentally (Sallam et al., 2002).

6.5 Ligament Rupture

Having analyzed the mechanisms through which ligaments are generated, the rupture of these ligaments should now be characterized more precisely. Two potential processes are competing to break the ligaments and form droplets, namely, the classical Rayleigh breakup (i.e., the capillary breakup of a liquid cylinder) and aerodynamic forces acting on the ligaments (i.e., secondary atomiza-

tion). The idea that primary and secondary breakups merge and interact together for low-density ratios has been introduced previously (see, e.g., Faeth et al., 1995. Ranger and Nicholls (1969) and Hsiang and Faeth (1992) presented the mechanisms by which a droplet undergoes secondary atomization, and Wu and Faeth (1993) suggested that this process could affect liquid structures during primary atomization itself. It has already been clearly established that the cases considered here are strongly affected by aerodynamic forces; therefore, it is likely that these forces will contribute to the rupture of the ligaments that they helped forming. Wu and Faeth (1993) provided a phenomenological formula for the ratio of the Rayleigh breakup time scale τ_R to the aerodynamic breakup time scale τ_A that is based on the distance from the injection and the local turbulent Weber number. Following the work of Hsiang and Faeth (1992), the time scale associated with aerodynamic breakup of a liquid structure of size L moving at U_0 in still gas can be expressed as $\tau_A = \sqrt{\rho_l/\rho_g}L/U_0$. Similarly, Rayleigh breakup can classically be characterized by $\tau_R = \sqrt{\rho_l L^3/\sigma}$. The smallest time scale should correspond to the main mechanism by which ligament breakup occurs. The ratio of these time scales can be expressed by $\tau_A/\tau_R = \mathrm{We}_{L,g}^{-1/2}$, where $\mathrm{We}_{L,g} = \rho_g U_0^2 L/\sigma$ is a Weber number based on the gas density and the liquid protrusion size. Two conclusions can be drawn from this time-scale analysis: the higher the surface tension force is, the more likely it is for breakup to be due to capillary instabilities, and the larger the liquid structures are, the more likely it is for breakup to originate from aerodynamic forces. Recall that in the present simulations liquid, structures tend to become larger with time. This observation can be related to the time it takes to develop larger corrugations, and also to the increase of the turbulent scales with time. Consequently, it can be expected that Rayleigh breakup should dominate early on, whereas at later times aerodynamic effects could lead to merged primary/secondary breakup, especially for high Weber number cases. Case $TPb1$ displays the two types of ligament breakup. Figure 19(a) shows classical Rayleigh breakup of a ligament early in the simulation, leading to the formation of three droplets. Figure 19(b) shows the breakup of a ligament aligned in the spanwise direction. In this case, it is unclear what

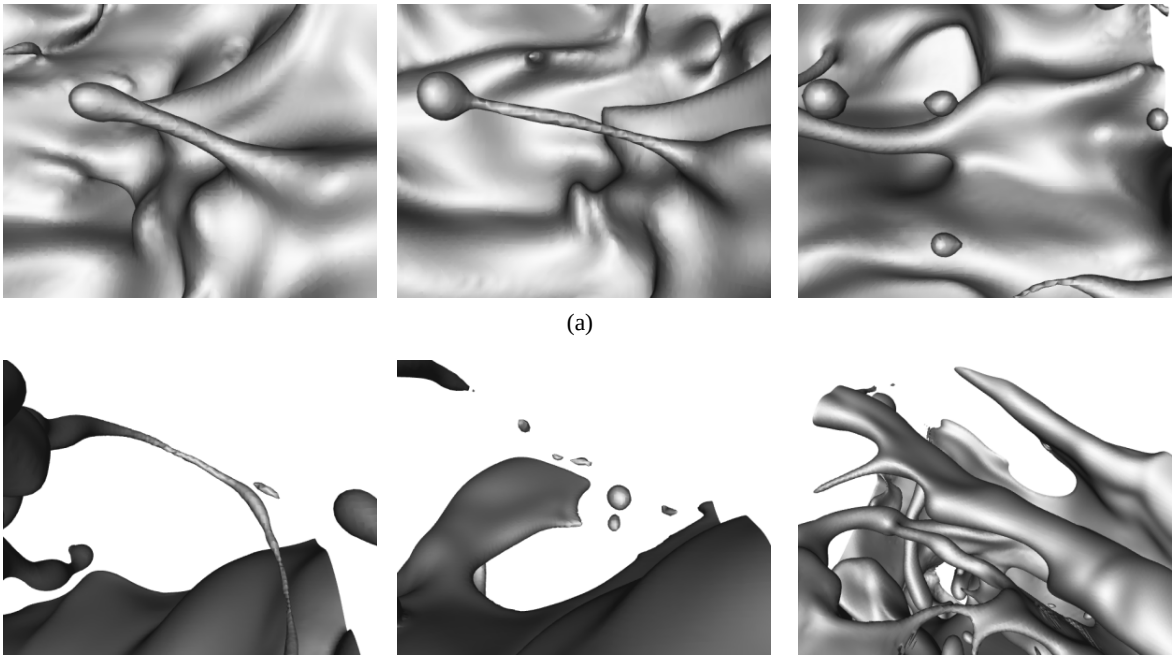

(a) (b) (c)

FIG. 19: Sample ligament breakup events for case $TPb1$. (a) Rayleigh breakup of a ligament. Note that on the rightmost picture, the bottom droplet is not associated with the breakup of the ligament followed here. (b) Breakup of a ligament misaligned with the flow. (c) Aerodynamic stripping of a ligament. On the large ligament extending from the top left corner of the picture to the bottom right corner, secondary ligaments can be seen developing.

the main mechanism for breakup is because aerodynamic forces acting on a ligament misaligned with the mean flow direction should be intense. Finally, Fig. 19(c) shows a clear aerodynamic stripping of a large ligament, leading to the creation of secondary bulges and ligaments.

6.6 Detailed Liquid Structures

6.6.1 Bubble Entrapment

Early in the simulations, the wall-bounded nature of the turbulent flow leads to frequent entrapment of air bubbles. In wall-bounded flows, two counter rotating vortex streaks close to each other lead to a local sweep effect, followed by an ejection phenomenon where fluid is rapidly displaced away from the wall (Kim, 1983; Kim and Moin, 1986; Kim et al., 1987). A similar process is encountered here, except that the phase-interface is being deformed in the process. Figure 20 illustrates this process by showing the phase-interface as well as an iso-surface of Q-criterion colored by the axial vorticity. Streaks that are formed in the nozzle flow survive during the early times of the jet development. The interface is pinched between these two counter-rotating vortices, eventually forming an air pocket in the liquid. This process is similar to the ejections in wall-bounded flows, except that in the presence of a deformable interface, the streaks tend to engulf the gas in the liquid, which can create elongated air structures that penetrate significantly inside the liquid. When these structures eventually break, air bubbles remain in the liquid jet.

6.6.2 Bubble Bursting

The air bubbles that have been entrapped in the liquid are found to occasionally break the liquid surface. When this occurs, the interface first bulges because of the rising bubble, which is shown in Fig. 21. Then, the thin liquid layer ruptures and a crater is formed. As the remaining liquid lip recedes, a vortex is formed that leads to the generation of a central jet. The event shown in Fig. 21 does not have any lasting consequence on the interface evolution. However, it contributes to the overall destabilization of the jet. In other cases, events of the same nature were found to have a significant influence on the evolution of the jet. In the case where the air bubble engulfed in the liquid has an elongated shape, the crater that is formed when the bubble breaks the liquid surface has a very high curvature. Such a high local curvature induces a strong acceleration, which can lead to the formation of a very intense liquid jet. If the jet is strong enough, a ligament is formed, and shear will contribute to its elongation, eventually leading to its rupture and to the formation of liquid droplets. This mechanism of ligament formation has been observed several times in these simulations, and such an event is shown in Fig. 22. Although it is accepted that bubble bursting can lead to droplet formation (Duchemin et al., 2002; Herrmann, 2005), this is the first time this mechanism is identified as a droplet generation mechanism in the turbulent atomization of liquid jets.

6.6.3 Ligament–Ligament Collision

Although droplet collisions have been extensively studied both experimentally and numerically (Ashgriz and Poo, 1990; Tanguy and Berlemont, 2005), and are expected to take place frequently provided the droplet number density is high, the simulations conducted in this work also display frequent ligament collisions. Indeed, the intense fingering of the liquid for the high Weber cases lead to a high density of ligaments at the jet surface. As stated

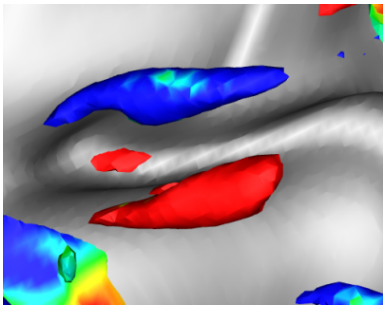

(a) Pinching of the interface between two counter-rotating vortices.

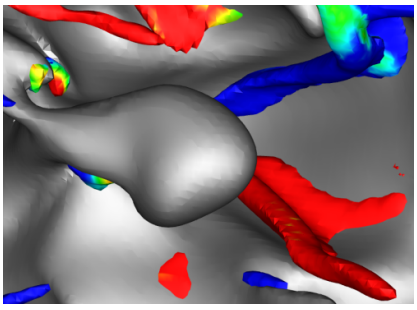

(b) Engulfment of air through local ejection.

FIG. 20: Engulfment of air bubbles in the liquid by local ejection. Interface viewed from the liquid side, and iso-surface of Q-criterion colored by the axial vorticity.

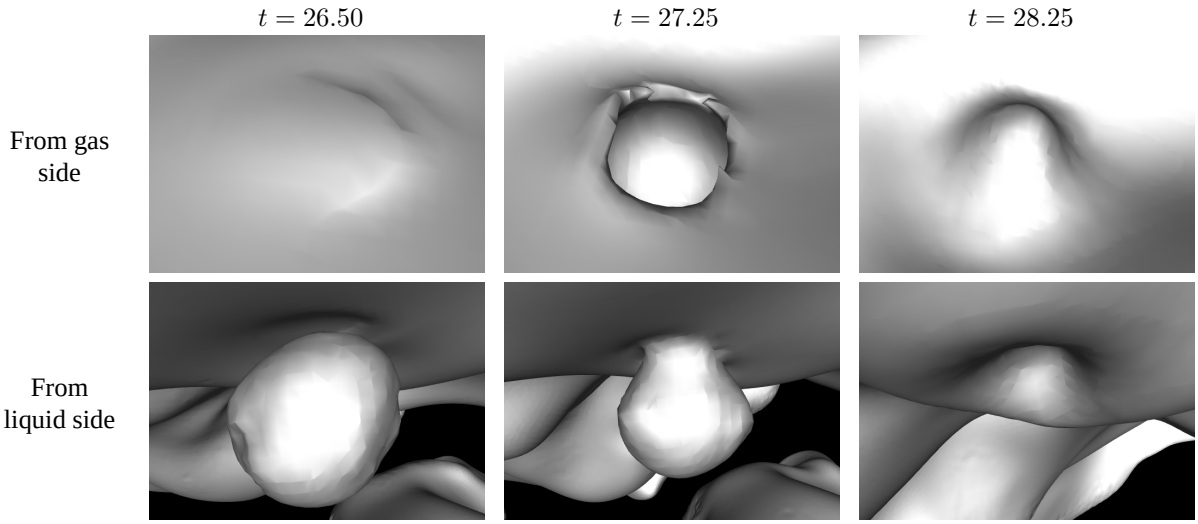

FIG. 21: Example of bubble bursting with limited consequences on the interface.

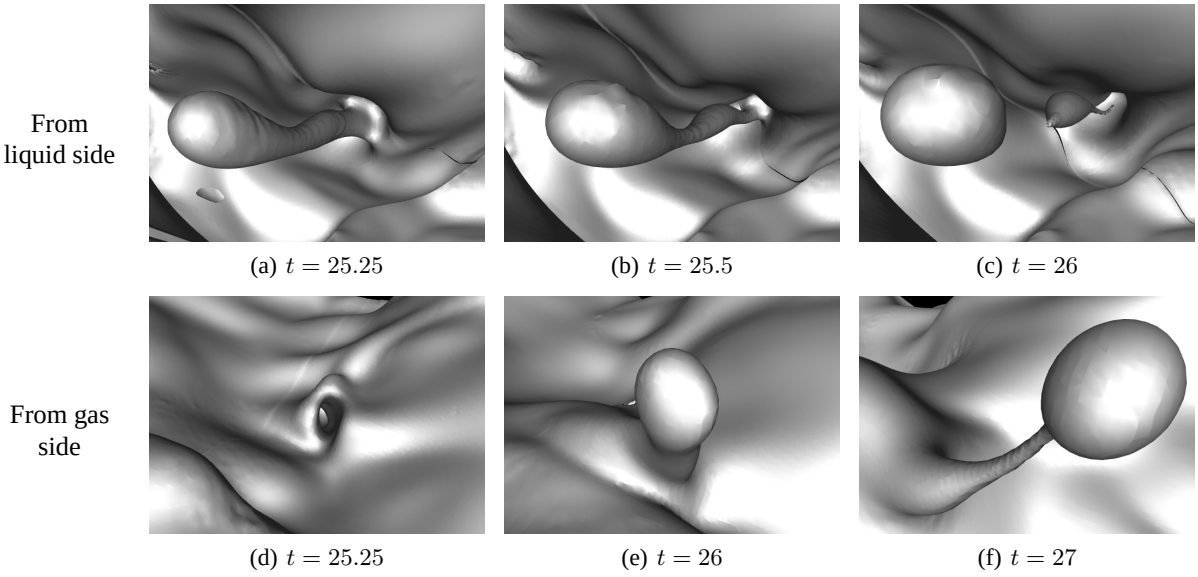

(a) $t = 25.25$ (b) $t = 25.5$ (c) $t = 26$

(d) $t = 25.25$ (e) $t = 26$ (f) $t = 27$

FIG. 22: Example of bubble bursting with ligament generation.

earlier, the aerodynamic forces on these ligaments can be significant and can be affected by surrounding turbulence. These ligaments are therefore likely to interact and collide, leading to various outcomes as in the case of binary droplet collisions. An example is shown in Fig. 23, where two ligaments rupture during their collision, leading to the formation of several droplets. Another possible outcome of ligament collisions is the formation of liquid bridges. Two examples of such liquid bridges are shown in Fig. 24, where both bridges parallel to the flow and bridges perpendicular to the flow are observed.

6.6.4 Droplet Splashing

Finally, frequent occurrences of the splashing of a detached droplet onto the inner liquid core are observed. In many instances, these events follow the classical droplet splashing, described extensively in the review by Yarin (2006). Figure 25 shows an example of splashing, with the expected formation of a crater. Often, little consequence on the interface shape was observed. However, in several instances, the interaction between a droplet and the liquid core was found to initiate the formation of lig-

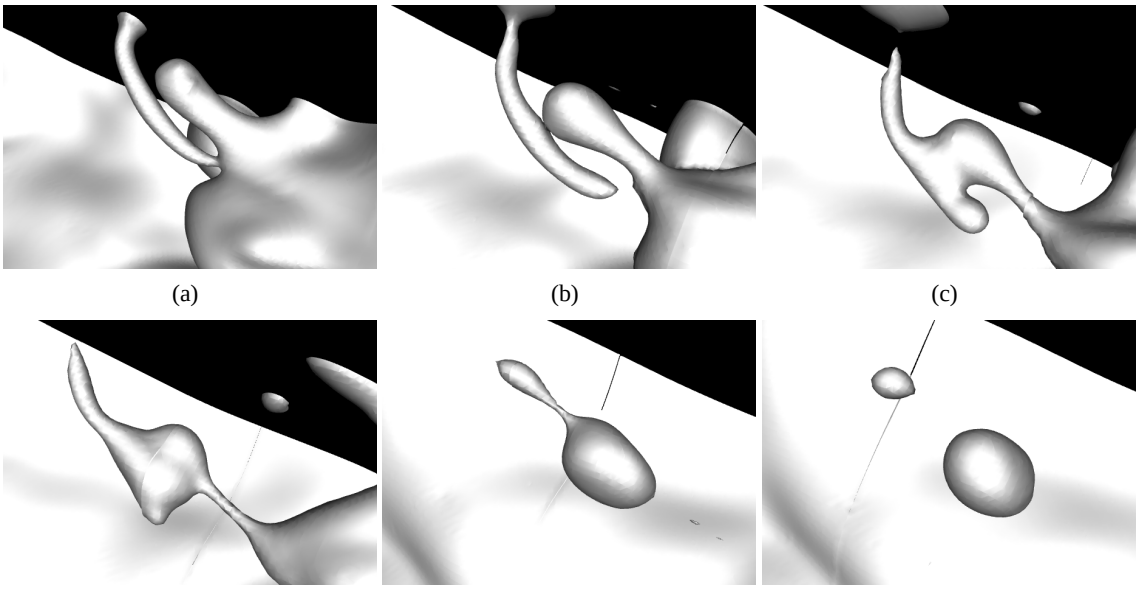

(a) (b) (c)

(d) (e) (f)

FIG. 23: Ligament collision leading to breakup, viewed from the gas side.

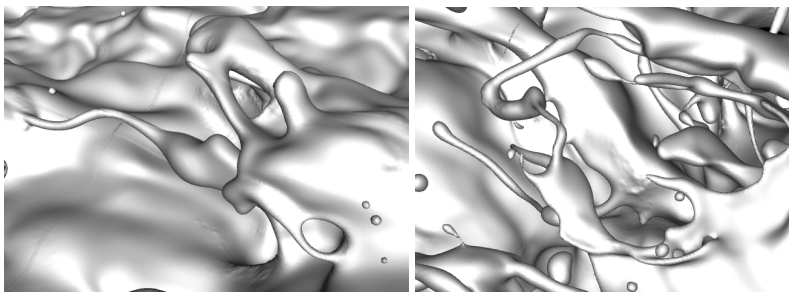

(a) We $= 500$ (b) We $= 2000$

FIG. 24: Example of bridges formed by way of ligament collision for various Weber numbers, viewed from the gas side.

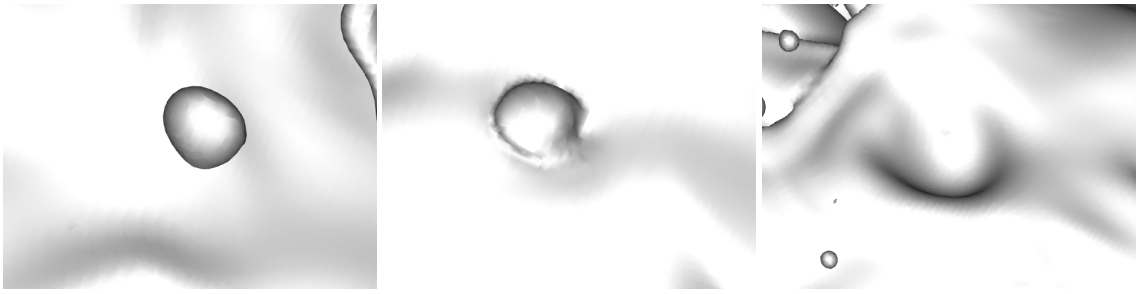

(a) (b) (c)

FIG. 25: Example of droplet splashing with limited consequences on the interface, viewed from the gas side.

aments, such as shown in Fig. 26. Note that the event depicted in Fig. 26 does not follow the accepted splashing mechanism. Instead, it involves a droplet moving almost tangentially with respect to the interface.

This list of detailed interface behaviors suggests that when aerodynamic forces play a role, the combined effect of turbulence, ligament generation and collision, and bubble entrapment leads to a very complex atomization process. Although ligament formation followed by Rayleigh breakup seems to be the major path through which droplets are generated, it clearly appears that highly complex ligament interactions might lead to early ligament rupture and therefore might significantly affect drop size distribution. Note that the simulation results identified the interaction between the liquid core and bubbles or droplets as possible, although potentially marginal, mechanisms through which ligaments can be created.

7. CONCLUSION

This work attempts to improve the understanding of primary atomization through detailed numerical simulations. Numerical techniques have matured rapidly in the past few years, and the associated increase in computational power allows one to perform fine simulations of complex turbulent problems. By carefully choosing the simulation parameters, turbulent atomization can be simulated, with reasonable confidence in the numerics. This work is considered a first step toward realistic applications. The density ratio employed is similar to that of diesel injection. The Reynolds number is slightly reduced compared to realistic injectors, however, still of the right order of magnitude. The Weber number is reduced manyfold in order to make the liquid structures tractable. This numerical study provides a wealth of much-needed detailed information on the turbulent atomization process, which is invaluable to large-eddy simulation modeling. Careful analysis of the results suggests that aerodynamic effects play a significant role in the turbulent atomization of liquid jets. Several detailed mechanisms have been identified, such as bubble formation through sweep-ejection events and ligament generation due to bubble bursting or droplet collision.

ACKNOWLEDGMENTS

The authors wish to express their gratitude to Dr. Guillaume Balarac for many helpful discussions about this work. We also gratefully acknowledge funding by NASA and by the DOE through the ASC program.

REFERENCES

Ashgriz, N. and Poo, J. Y., Coalescence and separation in binary collisions of liquid drops, *J. Fluid Mech.*, vol. 221, pp. 183–204, 1990.

Bianchi, G. M., Minelli, F., Scardovelli, R., and Zaleski, S., 3D large scale simulation of the high-speed liquid jet atomization, SAE Paper No. 2007-01-0244, 2007.

Bianchi, G. M., Pelloni, P., Toninel, S., Scardovelli, R., Leboissetier, A., and Zaleski, S., Improving the knowledge of high-speed liquid jets atomization by using quasi-direct 3D simulation, SAE Paper No. 2005-24-089, 2005.

Boeck, T. and Zaleski, S., Viscous versus inviscid instability of two-phase mixing layers with continuous velocity profile, *Phys. Fluids*, vol. 17, pp. 032106-1–032106-11, 2005.

Chou, W. H. and Faeth, G. M, Temporal properties of secondary drop breakup in the bag breakup regime, *Int. J. Multiphase Flow*, vol. 24, no. 6, pp. 889–912, 1998.

Da Silva, C. B. and Pereira, J. C. F., The effect of subgrid-scale models on the vortices computed from large-eddy simulations, *Phys. Fluids*, vol. 16, pp. 4506–4534, 2004.

De Villiers, E. and Gosman, D., Large eddy simulation of pri-

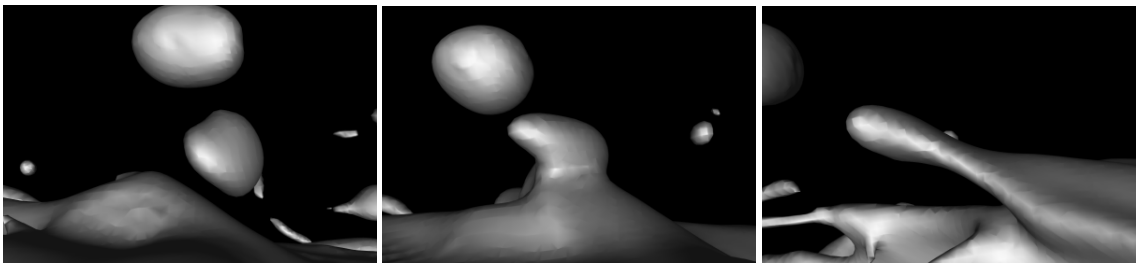

(a) (b) (c)

FIG. 26: Example of a detached droplet interacting with the liquid core, leading to ligament generation, viewed from the gas side.

mary Diesel spray atomization, SAE Paper No. 2004-01-0100, 2004.

Desjardins, O., Blanquart, G., Balarac, G., and Pitsch, H., High order conservative finite difference scheme for variable density low Mach number turbulent flows, *J. Comput. Phys.*, vol. 227, no. 15, pp. 7125–7159, 2008a.

Desjardins, O., Moureau, V., and Pitsch, H., An accurate conservative level set/ghost fluid method for simulating primary atomization, *J. Comput. Phys.*, vol. 227, no. 18, pp. 8395–8416, 2008b.

Desjardins, O. and Pitsch, H., Modeling effect of spray evaporation on turbulent combustion, *10th International Congress on Liquid Atomization and Spray Systems*, Kyoto, Japan, 2006.

Desjardins, O. and Pitsch, H., A spectrally refined interface approach for simulating multiphase flows, *J. Comput. Phys.*, vol. 228, no. 5, pp. 1658–1677, 2009.

Dubief, Y. and Delcayre, F., On coherent-vortex identification in turbulence, *J. Turbul.*, vol. 1, pp. 1–22, 2000.

Duchemin, L., Popinet, S., Josserand, C., and Zaleski, S., Jet formation in bubbles bursting at a free surface, *Phys. Fluids*, vol. 14, no. 9, pp. 3000–3008, 2002.

Faeth, G. M., Hsiang, L. P., and Wu, P. K., Structure and breakup properties of sprays, *Int. J. Multiphase Flow*, vol. 21, pp. 99–127, 1995.

Fedkiw, R., Aslam, T., Merriman, B., and Osher, S., A nonoscillatory Eulerian approach to interfaces in multimaterial flows (the ghost fluid method), *J. Comput. Phys.*, vol. 152, pp. 457–492, 1999.

Gorokhovski, M., The stochastic sub-grid-scale approach for spray atomization, *Atomization and Sprays*, vol. 11, pp. 505–519, 2001.

Gorokhovski, M. and Herrmann, M., Modeling primary atomization, *Ann. Rev. Fluid Mech.*, vol. 40, pp. 343–366, 2008.

Herrmann, M., Refined level set grid method for tracking interfaces, *Annual Research Briefs*, Center for Turbulence Research, Stanford, CA, 2005.

Hsiang, L. P. and Faeth, G. M., Near-limit drop deformation and secondary breakup, *Int. J. Multiphase Flow*, vol. 18, no. 5, pp. 635–652, 1992.

Hunt, J. C. R., Wray, A. A., and Moin, P., Eddies, streams and convergence zones in turbulent flows, Tech. Rep. No. CTR-S88. Center for Turbulence Research, 1988.

Kim, J., On the structure of wall-bounded turbulent flows, *Phys. Fluids*, vol. 26, pp. 2088–2097, 1983.

Kim, J. and Moin, P., The structure of the vorticity field in turbulent channel flow. II. Study of ensemble-averaged fields, *J. Fluid Mech.*, vol. 162, pp. 339–363, 1986.

Kim, J., Moin, P., and Moser, R., Turbulence statistics in fully developed channel flow at low Reynolds number, *J. Fluid Mech.*, vol. 177, pp. 133–166, 1987.

Knudsen, E. and Pitsch, H., A dynamic model for the turbulent burning velocity for large eddy simulation of premixed combustion, *Combust. Flame*, vol. 154, no. 4, pp. 740–760, 2008.

Knudsen, E. and Pitsch, H., A general amelet transformation useful for distinguishing between premixed and nonpremixed modes of combustion, *Combust. Flame*, vol. 156, no. 3, pp. 678–696, 2009.

Kong, S. C., Senecal, P. K., and Reitz, R. D., Developments in spray modelling in Diesel and direct-injection gasoline engines, *Oil Gas Sci. Tech. Rev. IFP*, vol. 54, pp. 197–204, 1999.

Lasheras, J. C. and Hopfinger, E. J., Liquid jet instability and atomization in a coaxial gas stream, *Ann. Rev. Fluid. Mech.*, vol. 32, pp. 275–308, 2000.

Lefebvre, A. H., *Atomization and Spray*, Taylor and Francis, New York, 1989.

Levich, V. G., *Physico-Chemical Hydrodynamics*, Prentice-Hall, Englewood Cliffs, NJ, 1992.

Marmottant, P. and Villermaux, E., On spray formation, *J. Fluid Mech.*, vol. 498, pp. 73–112, 2004.

Ménard, T., Tanguy, S. and Berlemont, A., Coupling level set/VOF/ghost uid methods: Validation and application to 3D simulation of the primary break-up of a liquid jet, *Int. J. Multiphase Flow*, vol. 33, pp. 510–524, 2007.

Miesse, C. C., Correlation of experimental data on the disintegration of liquid jets, *Ind. Eng. Chem.*, vol. 47, pp. 1690–1701, 1955.

Ohnesorge, W., Formation of drops by nozzles and the breakup of liquid jets, *Z. Angew. Math. Mech.*, vol. 16, pp. 355–358, 1936.

Pan, Y. and Suga, K., A numerical study on the breakup process of laminar liquid jets into a gas, *Phys. Fluids*, vol. 18, pp. 052101-1–052101-11, 2006.

Park, M., Yoo, J. Y., and Choi, H., Discretization errors in large eddy simulation: On the suitability of centered and upwind-biased compact difference schemes, *J. Comput. Phys.*, vol. 198, pp. 580–616, 2004.

Patterson, M. A. and Reitz, R. D., Modeling the effects of fuel spray characteristics on Diesel engine combustion and emissions, SAE Tech. Paper No. 980131, 1998.

Pierce, C. D. and Moin, P., Progress-variable approach for large eddy simulation of turbu- lent combustion, Tech. Rep. No. TF80, Flow Physics and Computation Division, Dept. Mech. Eng., Stanford University, 2001.

Ranger, A. A. and Nicholls, J. A., Aerodynamic shattering of liquid drops, *J. AIAA*, vol. 7, pp. 285–290, 1969.

Reitz, R. D., Atomization and other breakup regimes of a liquid jet, PhD thesis, Princeton University, 1978.

Sallam, K. A., Dai, Z., and Faeth, G. M., Drop formation at the surface of plane turbulent liquid jets in still gases, *Int. J.*

Multiphase Flow, vol. 25, no. 6, pp. 1161–1180, 1999.

Sallam, K. A., Dai, Z., and Faeth, G. M., Liquid breakup at the surface of turbulent round liquid jets in still gases, *Int. J. Multiphase Flow*, vol. 28, no. 3, pp. 427–449, 2002.

Smallwood, G. and Gülder, Ö, Views on the structure of transient Diesel spray, *Atomization and Sprays*, vol. 10, pp. 355–386, 2000.

Stanley, S. A., Sarkar, S., and Mellado, J. P., A study of the flow-field evolution and mixing in a planar turbulent jet using direct numerical simulation, *J. Fluid. Mech.*, vol. 450, pp. 377–407, 2002.

Tanguy, S. and Berlemont, A., Application of a level set method for simulation of droplet collisions, *Int. J. Multiphase Flow*, vol. 31, pp. 1015–1035, 2005.

Taylor, G. I., Cavitation of viscous uid in narrow passages, *J. Fluid Mech*., vol. 16, pp. 595–619, 1963.

Vallet, A., Burluka, A., and Borghi, R., Development of an Eulerian model for the atomization of a liquid jet, *Atomization and Sprays*, vol. 11, pp. 619–642, 2001.

Villermaux, E., Fragmentation, *Ann. Rev. Fluid. Mech.*, vol. 39, pp. 419–446, 2007.

Wang, L. and Pitsch, H., Prediction of pollutant emissions from industrial furnaces using large eddy simulation, *5th U.S. Combustion Meeting*, San Diego, 2007.

Wang, Y., Liu, X., Im, K.-S., Lee, W.-K., Wang, J., Fezzaa, K., Hung, D. L. S., and Winkelman, J. R., Ultrafast x-ray study of dense-liquid-jet ow dynamics using structure-tracking velocimetry, *Nature Physics*, vol. 4, pp. 305–309, 2008.

Wu, P. K. and Faeth, G. M., Aerodynamic effects on primary breakup of turbulent liquids, *Atomization and Sprays*, vol. 3, no. 3, pp. 265–289, 1993.

Yarin, A. L., Drop impact dynamics: Splashing, spreading, receding, bouncing..., *Ann. Rev. Fluid. Mech.*, vol. 38, pp. 159–192, 2006.

Yecko, P., Zaleski, S., and Fullana, J.-M., Viscous modes in two-phase mixing layers, *Phys. Fluids*, vol. 14, pp. 4115–4122, 2002.

Yi, Y. and Reitz, R. D., Modeling the primary break-up of high-speed jets, *Atomization and Sprays*, vol. 14, pp. 53–80, 2004.